Suppression of transcytosis regulates zebrafish blood-brain barrier development

Natasha M. O'Brown[1], Sean G. Megason[2*], Chenghua Gu[1*]

[1] Department of Neurobiology, [2] Department of Systems Biology, Harvard Medical School, 220 Longwood Ave, Boston, MA 02115, U.S.A.

* denotes corresponding author

Correspondence:

Chenghua Gu (chenghua_gu@hms.harvard.edu)

Department of Neurobiology, Harvard Medical School

Boston, MA 02115, U.S.A.

(Phone) 617-432-6364 (Fax) 617-432-1639

Sean Megason (sean_megason@hms.harvard.edu)

Department of Systems Biology, Harvard Medical School

Boston, MA 02115, U.S.A.

(Phone) 617-432-7441

Abstract:

As an optically transparent model organism with an endothelial blood-brain barrier (BBB), zebrafish offer a powerful tool to study the vertebrate BBB. However, the precise developmental profile of functional zebrafish BBB acquisition and the subcellular and molecular mechanisms governing the zebrafish BBB remain poorly characterized. Here we find a spatiotemporal gradient of barrier acquisition. Moreover, we capture the dynamics of developmental BBB leakage using live imaging, revealing a combination of steady accumulation in the parenchyma and sporadic bursts of tracer leakage. Electron microscopy studies further reveal that this steady accumulation results from high levels of transcytosis that are eventually suppressed, sealing the BBB. Finally, we demonstrate a key mammalian BBB regulator Mfsd2a, which inhibits transcytosis, plays a conserved role in zebrafish. *Mfsd2aa* mutants display increased larval and adult BBB permeability due to increased transcytosis. Our findings indicate a conserved developmental program of barrier acquisition between zebrafish and mice.

Introduction

Blood vessels in the vertebrate brain are composed of a single layer of endothelial cells that possess distinct functional properties that allow the passage of necessary nutrients yet prevent unwanted entry of specific toxins and pathogens into the brain. This specialized endothelial layer forms the blood-brain barrier (BBB) and restricts the passage of substances between the blood and the brain parenchyma via two primary mechanisms: 1) specialized tight junction complexes between apposed endothelial cells to prevent intercellular transit (Reese and Karnovsky, 1967; Brightman and Reese, 1969) and 2) suppressing vesicular trafficking or transcytosis to prevent transcellular transit (Ben-Zvi et al., 2014; Andreone et al., 2015; Andreone et al., 2017). BBB selectivity is further refined with expression of substrate-specific transporters that dynamically regulate the influx of necessary nutrients and efflux of metabolic waste products (Sanchez-Covarrubias et al., 2014; Umans et al., 2017). While the BBB is comprised of endothelial cells, the surrounding perivascular cells including pericytes and astroglial cells, play a critical role in forming and maintaining barrier properties (Janzer and Raff, 1987; Armulik et al., 2010; Bell et al., 2010; Daneman et al., 2010; Wang et al., 2014). Collectively, endothelial cells and the surrounding perivascular cells form the neurovascular unit.

As the simplest genetic model organism with an endothelial BBB (Jeong et al., 2008), zebrafish offer a powerful tool to study the cellular and molecular properties of the vertebrate BBB (Xie et al., 2010; Vanhollebeke et al., 2015; Umans et al., 2017; O'Brown et al., 2018; Quiñonez-Silvero et al., 2019). Zebrafish have served as a great model system to study vascular biology due to their large clutch size, rapid and external development, and transparency for *in vivo* whole organism live-imaging (Lawson and Weinstein, 2002; Jin et al., 2005; Santoro et al., 2007; Armer et al., 2009; Herbert et al., 2009; Phng et al., 2009; Geudens et al., 2010; Herbert et al., 2012; Wilkinson and van Eeden, 2014; Franco et al., 2015; Vanhollebeke et al., 2015; Matsuoka et al., 2016; Ulrich et al., 2016; Galanternik et al., 2017; Stratman et al., 2017; Geudens et al., 2018).

63 Additionally, with the advent of CRISPR-Cas9 technology, zebrafish provide an efficient genetic
64 toolkit for targeted mutagenesis (Hwang et al., 2013; Gagnon et al., 2014; Ablain et al., 2015;
65 Varshney et al., 2015; Albadri et al., 2017; Hogan and Schulte-Merker, 2017). However, the
66 subcellular and molecular mechanisms governing the formation and maintenance of the zebrafish
67 BBB remain poorly characterized. Expanding our understanding of the zebrafish BBB can thus
68 reveal the mechanistic similarities between the zebrafish and mammalian BBB to further elevate
69 the position of zebrafish as a model organism for studying the BBB.
70
71 Barrier properties of brain endothelial cells are induced by extrinsic signals from other cells in the
72 surrounding microenvironment during development (Stewart and Wiley, 1981). In rodents, the
73 BBB becomes functionally sealed in a spatiotemporal gradient, with the hindbrain and midbrain
74 barriers becoming functional before the cortical barrier (Daneman et al., 2010; Ben-Zvi et al.,
75 2014; Sohet et al., 2015). Within the cortex, barrier function is acquired along a ventral-lateral to
76 dorsal-medial gradient (Ben-Zvi et al., 2014). In the zebrafish, existing studies have disagreed
77 over the timing of zebrafish barrier formation, with some suggesting that BBB maturation occurs
78 at 3 days post fertilization (dpf) (Jeong et al., 2008; Umans et al., 2017) and others providing a
79 wide range beginning at 3 dpf and extending to 10 dpf (Fleming et al., 2013). These conflicting
80 reports may be due to regional developmental gradients of barrier acquisition or differences in the
81 experimental approaches used to assess BBB permeability such as the molecular weight of
82 tracers and circulation time. To date, a thorough regional characterization of functional barrier
83 acquisition has been lacking in zebrafish.
84
85 Recent work in the mammalian blood-retinal barrier has indicated that suppression of transcytosis
86 governs functional barrier development (Chow and Gu, 2017). Interestingly endothelial cells at
87 the leaky neonatal angiogenic front possess functional tight junction complexes halting the
88 intercellular passage of the tracer protein Horseradish Peroxidase (HRP) at the so-called “kissing

89 points". In contrast, these endothelial cells exhibit high levels of HRP-filled vesicles compared to
90 functionally sealed proximal vessels. Moreover, these areas of elevated vesicular trafficking
91 continue to correspond with barrier permeability at the angiogenic front until the barrier seals
92 (Chow and Gu, 2017). Work in the mouse BBB has also demonstrated the importance of
93 suppressing transcytosis in determining barrier permeability. Mice lacking the major facilitator
94 super family domain containing 2a (Mfsd2a) lipid transporter exhibit increased levels of caveolae
95 vesicles in CNS endothelial cells, resulting in increased barrier permeability (Ben-Zvi et al., 2014;
96 Andreone et al., 2017). The subcellular and molecular mechanisms of zebrafish BBB acquisition
97 have yet to be elucidated.
98
99 Here in zebrafish, we find a spatiotemporal gradient of barrier acquisition, and capture the
100 dynamics of developmental BBB leakage using time lapse live imaging. We further find a
101 conserved role for transcytosis suppression in determining barrier properties, both during normal
102 development and in *mfsd2aa* mutants.
103
104 **Results**
105 *Posterior-Anterior Gradient of Zebrafish BBB Development*
106 To determine when and how the zebrafish BBB becomes functional in different brain regions, we
107 performed intracardiac injections of fluorescently-conjugated tracers (1 kDa NHS and 10 kDa
108 Dextran) simultaneously at different developmental stages and imaged live fish after one hour of
109 tracer circulation (Figure 1A and 1B). We used a combination of different molecular weight tracers
110 to tease apart potential avenues of leakage, as tight junctional defects result specifically in the
111 leakage of low molecular weight tracers 1 kDa and below into the brain parenchyma (Nitta et al.,
112 2003; Campbell et al. 2008; Sohet et al., 2015; Yanagida et al. 2017). At 3 dpf, we observed a
113 sealed barrier in the hindbrain as previously described (Jeong et al., 2008), with only a few of the
114 parenchymal cells taking up the injected tracer (average of 2 ± 0.3 cells/embryo with NHS and 2

115 ± 0.4 cells/embryo with Dextran; Figure 1 – Supplement 1), which we quantify as a proxy of tracer
116 leakage into the brain. However, in the midbrain we observed an increased number of
117 parenchymal cells that accumulated the circulating tracers (average of 24 ± 1 cells/embryo with
118 NHS and 24 ± 1 cells/embryo with Dextran; Figure 1C and 1D), indicating that the tracers leaked
119 out of the blood vessels into the brain and that the midbrain barrier is not yet functional. In addition
120 to the use of exogenous injected fluorescent tracers, we also assayed BBB permeability with an
121 endogenous transgenic serum DBP-EGFP fusion protein (Tg(*l-fabp:DBP-EGFP*)) to account for
122 injection artifacts (Xie et al., 2010). At 3 dpf, we observed similar leakage patterns with the
123 transgenic serum protein as we did with the injected tracers (average of 24 ± 1 cells/embryo in
124 the midbrain and average of 2 ± 0.4 cells/embryo in the hindbrain; Figure 1C and D; Figure 1 –
125 Supplement 1). At 4 dpf, the BBB in the hindbrain is completely functional with few tracer-filled
126 parenchymal cells (average of 3 ± 0.4 cells/embryo with NHS, 2 ± 0.4 cells/embryo with Dextran
127 and DBP-EGFP; Figure 1 – Supplement 1). However, the midbrain BBB remains leaky (average
128 of 23 ± 1 cells/embryo with NHS and DBP-EGFP and 24 ± 1 cells/embryo with Dextran; $p=0.68$
129 compared to 3 dpf, one-way ANOVA; Figure 1C and 1D). However, at 5 dpf the number of
130 midbrain parenchymal cells that uptake the tracers is dramatically reduced (average of 9 ± 1
131 cells/embryo with NHS, Dextran, and DBP-EGFP; $p<0.0001$, one-way ANOVA; Figure 1B and
132 1C) and no change was observed in the hindbrain (Figure 1 – Supplement 1). No significant
133 change was observed in midbrain permeability from 5 to 6 dpf (average of 8 ± 1 cells/embryo with
134 NHS, Dextran, and DBP-EGFP; $p=0.904$, one-way ANOVA; Figure 1C and 1D), indicating that
135 the midbrain barrier becomes sealed at 5 dpf. We did not assay the forebrain at any of these
136 stages due to the fact that it remains avascularized until 5 dpf. Of note, all three tracers showed
137 nearly indistinguishable patterns of uptake, with similar numbers of cells and many of the same
138 cells simultaneously taking up both injected tracers (Figure 1; Figure 1 – Supplement), suggesting

139 that the leakage is not due to tight junctional defects but may rather be due to an increase in
140 vesicular trafficking.

141 *Time lapse Imaging Reveals Two Modes of Developmental Leakage*

142 The vast majority of studies interrogating BBB permeability have relied on observing leakage in
143 fixed static images from mutant mice, which does not reveal the dynamic nature of the BBB. A
144 huge advantage of zebrafish is the ability to examine biological processes *in vivo* in real-time,
145 providing us with the unique opportunity to observe the process of BBB maturation (Figure 1). To
146 examine the developmental dynamics of barrier leakage, we injected embryos at 3 dpf with
147 fluorescently-labeled 10 kDa Dextran and performed time lapse live imaging for an hour following
148 injection, with time 0 being an average of 8 minutes post-injection. We observed a gradual and
149 diffuse increase in extravascular Dextran intensity over time within the brain parenchyma (slope
150 of 1.301e-4 intensity/sec; Videos 1 and 2; Figure 2A, 2C and 2E). In addition to the time-
151 dependent increase in overall Dextran intensity in the brain parenchyma, we also observed
152 parenchymal cells taking up tracer, both directly adjacent to blood vessels and at a small distance
153 away (Figure 2A and 2C), as in the static images of tracer leakage during development (Figure
154 1). Interestingly, at 3 dpf we observed an actively sprouting cell that extended away from the
155 established vessel in a sporadic fashion (Video 2; Figure 2A). After twenty minutes of rambling
156 migration, this sprout suddenly released a large bolus of Dextran that appeared to be taken up by
157 a single parenchymal cell. Two minutes later, this same sprout released a second bolus of Dextran
158 on the opposite side (Video 2). These rare large bursts of leakage were not unique to this sprout;
159 they were also sporadically observed from established blood vessels (Video 1; Figure 2A). This
160 data revealed two types of leakage occurring during this early developmental stage: steady and
161 diffuse Dextran leakage into the parenchyma that makes up the vast majority of observed leakage
162 and rare large bursts of leakage. When we performed these same time lapse experiments at 5
163 dpf, we observed significantly less overall tracer accumulation in the brain parenchyma over the
164 course of the hour in addition to reduced rates of tracer accumulation (slope of 4.641e-5

165 intensity/sec; Video 3; $p<0.001$, Mann-Whitney test; Figure 2B, 2D and 2E). Furthermore, 5 dpf
166 fish never exhibited bursts of tracer leakage as observed at 3 dpf. Overall, 5 dpf fish had far fewer
167 parenchymal cells filling with Dextran than at 3 dpf, as observed in the static tracer leakage assays
168 (Figure 1). We interpret these data to suggest that at early stages, most tracer leakage occurs
169 broadly through vessel walls potentially via unrestricted transcytosis with an occasional transient
170 rupture to endothelial integrity that lead to these large bursts of leakage. Once tracer is leaked
171 into the intercellular space of the parenchyma it is taken up by select parenchymal cells. As the
172 BBB matures both sources of leakage sharply decrease.
173
174 *Suppression of Transcytosis Governs BBB Development*
175 Given the observed differences in permeability during larval development, we next sought to
176 determine the subcellular mechanisms underlying the development of a functional BBB.
177 Therefore, we assessed BBB properties by performing intracardiac injections of electron-dense
178 NHS-gold nanoparticles (5 nm) followed by transmission electron microscopy (TEM) at different
179 developmental stages when the midbrain barrier is leaky (3 dpf) and when it is functionally sealed
180 to fluorescent tracers (5 and 7 dpf; Figure 3). All of the blood vessels analyzed had a maximal
181 diameter of 5 μm to enrich for capillaries and small veins. At 3 dpf, we found blood vessels in
182 direct contact with neurons and pericytes, with the pericytes sharing the endothelial basement
183 membrane (Figure 3A), as in the mammalian neurovascular unit. During this leaky developmental
184 stage, the endothelial basement membrane was filled with the electron-dense gold nanoparticles
185 (Figure 3A and 3B; turquoise arrowheads) with an average gold intensity of 1.29 ± 0.07 (luminal
186 gold intensity normalized to 1.0; Figure 3G), further demonstrating that the BBB is immature at 3
187 dpf. To decipher how the gold nanoparticles traverse from the lumen to the basement membrane,
188 we first looked at the tight junctions to see if the nanoparticles passed between apposed
189 endothelial cells. After careful examination, we observed that the nanoparticles were halted at the
190 "kissing points" between endothelial cells, indicating that tight junctions were functional prior to

formation of a functional BBB (49/49 functional tight junctions; Figure 3B; green arrowhead). As transcytosis has been implicated in the maturation of the blood-retinal barrier (Chow and Gu, 2017), we next examined the levels of luminal and abluminal flask-shaped vesicles filled with gold nanoparticles as a means of assessing transcytosis. Quantification of gold-filled luminal and abluminal flask-shaped vesicles revealed an average of 0.21 ± 0.03 and 0.17 ± 0.02 vesicles/μm, respectively (Figure 3H and 3I). These data reveal that the basement membrane becomes filled with gold nanoparticles via vesicular transport rather than intercellular passage between immature tight junctions.

When we repeated this assay at 5 dpf, when the barrier becomes less permeable to fluorescently conjugated tracers (Figures 1 and 2), we still observe close contacts between endothelial cells and pericytes (Figure 3C). At 5 dpf, the basement membrane was noticeably lacking gold particles as compared to 3 dpf (Figure 3D), with a reduced average gold intensity of 0.85 ± 0.02 (Figure 3G). Like at 3 dpf, the tight junctions remained functional at 5 dpf, based on their capacity to halt gold nanoparticles at the kissing points between neighboring endothelial cells (76/76 functional tight junctions; Figure 3D). However, the levels of vesicles both luminally and abluminally were notably decreased to 0.08 ± 0.01 and 0.07 ± 0.01 vesicles/μm, respectively ($p<0.001$ (luminal) and $p<0.0001$ (abluminal), nested one-way ANOVA; Figure 3H and 3I). At 7 dpf the neurovascular cellular interactions remained constant with endothelial cells in close contact with pericytes and neurons, and with an unfilled basement membrane (average gold intensity of 0.91 ± 0.02; Figure 3E and 3G). Importantly, the tight junctions remained functional (51/51 functional tight junctions), and the low vesicular densities observed at 5 dpf remained comparably low at 7 dpf with 0.07 ± 0.01 vesicles/μm, both luminally and abluminally (Figure 3F, 3H and 3I). Taken together with the fluorescent tracer data, our data suggests that the zebrafish BBB becomes functional at 5 dpf via suppression of vesicular trafficking.

217 *Conserved Role of Mfsd2a in Determining BBB Function*

218 Given the important role of suppressing transcytosis in determining the developmental maturation
219 of the zebrafish BBB, we wondered whether the key mammalian barrier regulator Mfsd2a, which
220 suppresses caveolae mediated transcytosis (Ben-Zvi et al., 2014; Andreone et al., 2017), plays a
221 conserved role in zebrafish. Zebrafish contain two paralogues of *Mfsd2a*, *mfsd2aa* and *mfsd2ab*.
222 *Mfsd2aa* is 61% identical to human *MFSD2A* and 62% identical to mouse *Mfsd2a* (Figure 4 –
223 Supplement 1A). *Mfsd2ab*, on the other hand, is 64% identical to human *MFSD2A* and mouse
224 *Mfsd2a* (Figure 4 – Supplement 1A). The two paralogues are only 68% identical to each other,
225 but they both contain the lipid binding domain that is critical for governing barrier properties (Figure
226 4 – Supplement 1A; Andreone et al., 2017). Given the lack of a clear paralogue that most closely
227 resembles *Mfsd2a*, we generated CRISPR mutants for both paralogues independently.
228 *Mfsd2aa*$^{hm37/hm37}$ mutants have a 7 bp deletion in exon 2 (Figure 4 – Supplement 1B) that is
229 predicted to lead to a premature stop codon at amino acid 82 (Figure 4 – Supplement 1A; black
230 box). Homozygous *mfsd2aa* mutants are viable and fertile. *Mfsd2ab*$^{hm38/hm38}$ mutants have a 19
231 bp deletion in exon 5 (Figure 4 – Supplement 1B) that is predicted to lead to a premature stop
232 codon at amino acid 175 (Figure 4 – Supplement 1A; black box). Homozygous *mfsd2ab* mutants
233 are also viable and fertile. Neither mutant displayed obvious angiogenic defects, similar to the
234 normal vasculature observed in mouse *Mfsd2a* mutants (Ben-Zvi et al., 2014).

235

236 To investigate whether either paralogue was necessary for barrier formation, we performed NHS
237 tracer injection assays as we did to identify the developmental timeline of barrier formation and
238 assayed for midbrain leakage at 5 dpf. In addition to the use of the exogenous injected fluorescent
239 tracer (1 kDa NHS), we also assayed the leakage of the endogenous transgenic serum DBP-
240 EGFP fusion protein (Tg(*l-fabp:DBP-EGFP*)). *Mfsd2aa* mutants displayed about a two-fold
241 increase in midbrain tracer-containing parenchymal cells, both for the injected 1 kDa NHS and
242 the endogenous serum transgene 80 kDa DBP-EGFP, at 5 dpf compared to wildtype sibling

243 controls (Figure 4). These data suggest that mfsd2aa plays a similar role to mouse Mfsd2a in
244 determining barrier properties. Conversely, *mfsd2ab* mutants displayed similarly low levels of
245 tracer-containing parenchymal cells to wildtype controls at 5 dpf in the midbrain (Figure 4 -
246 Supplement 2), indicating that mfsd2ab is dispensable for functional barrier formation. To see if
247 the loss of both paralogues resulted in increased barrier permeability, we investigated
248 *mfsd2aa*$^{hm37/hm37}$*; mfsd2ab*$^{hm38/hm38}$ double mutants for BBB permeability using the endogenous
249 serum DBP-EGFP fusion protein (Figure 4 - Supplement 3). While *mfsd2aa* single mutants
250 displayed the previously observed increase in barrier permeability and *mfsd2ab* single mutants
251 did not, *mfsd2aa*$^{hm37/hm37}$*; mfsd2ab*$^{hm38/hm38}$ double mutants displayed similar levels of increased
252 barrier permeability to the *mfsd2aa* single mutants (Figure 4 - Supplement 3). Taken together,
253 these data suggest that the two paralogues, while structurally similar, play different roles, with
254 zebrafish mfsd2aa and mammalian Mfsd2a sharing a conserved role in determining barrier
255 permeability.
256
257 Given the leakage phenotype in *mfsd2aa* mutants at 5 dpf, we next wanted to examine whether
258 the leakage phenotype persisted into adulthood. To address this, we performed retro-orbital
259 injections of HRP, which has been shown to be confined within the adult zebrafish brain
260 vasculature (Jeong et al., 2008), and allowed the HRP to circulate for 30 minutes. As expected,
261 the wildtype siblings retained the HRP within their blood vessels (Figure 5A). However, *mfsd2aa*
262 mutants exhibited HRP extravasation into the brain parenchyma (Figure 5B), suggesting that the
263 leakage phenotype was not limited to larval fish. Finally, to determine whether this increased
264 permeability was due to increased transcytosis as in *Mfsd2a* knockout mice, we measured
265 vesicular density in capillaries with luminal diameters less than 5 μm from adult mutant and
266 wildtype siblings using TEM. The *mfsd2aa* mutant blood vessels appeared morphologically
267 normal by TEM, composed of a thin single layer of endothelial cells in close contact with pericytes,
268 as observed in their wildtype siblings (Figure 5C and 5D). A closer examination of the endothelial

269 cells revealed electron-dense tight junction complexes between all apposed endothelial cells in
270 both wildtype and *mfsd2aa* mutant fish (Figure 5E and 5F). However, while wildtype fish display
271 similarly low levels of luminal (0.1 vesicles/μm) and abluminal (0.11 vesicles/μm) vesicular
272 densities to those observed at 7 dpf (Figure 5E- 5H), *mfsd2aa* mutant fish display a significant
273 increase in luminal and abluminal vesicular densities (0.29 and 0.27 vesicles/μm, respectively)
274 compared to wildtype siblings (Figure 5E-5H). Interestingly this increase in vesicular abundance
275 is even higher than that observed during early barrier development at 3 dpf (Figure 2). These data
276 also suggest that the increased tracer leakage observed in *mfsd2aa* mutants results from an
277 increase in vesicular trafficking across the BBB, further supporting a conserved role for mfsd2aa
278 in determining barrier properties. In contrast to *mfsd2aa* mutants, *mfsd2ab* mutants displayed
279 similar levels of abluminal and luminal vesicular pit density to wildtype siblings (Figure 5 -
280 Supplement 1), further demonstrating that the paralog *mfsd2ab* does not play a conserved role in
281 determining barrier properties in zebrafish.
282
283 **Discussion**
284 One of the major advantages to studying the BBB in zebrafish is the ability to perform live imaging
285 of tracer permeability dynamics. We provide some of the first data on the dynamics of immature
286 barrier leakage. At 3 dpf, we observed two types of leakage, the gradual overall increase in the
287 parenchyma and rare transient bursts, both from a migrating sprout and established blood
288 vessels. We attribute the gradual diffuse increase in parenchymal tracer uptake to the high levels
289 of vesicular trafficking observed in our TEM analyses in which the endothelial basement
290 membrane became filled with gold nanoparticles. Therefore, the parenchymal Dextran intensity
291 measurements provide a direct proxy for the rates of BBB transcytosis *in vivo*. The rarer bursts of
292 leakage, on the other hand, could be due to fleeting tight junctional ruptures between neighboring
293 endothelial cells rather than increased vesicular trafficking. As these events were extremely
294 scarce during our time lapse imaging, it would be nearly impossible to capture these potential

295 junctional breaches by TEM to confirm this hypothesis. However, with continuing advances in the
296 resolution of fluorescence microscopy, we could use zebrafish to resolve whether these two types
297 of leakage, gradual and bursting, proceed through the same or different subcellular routes into
298 the brain parenchyma, either paracellularly or transcellularly.
299
300 Among the various clathrin-independent transcytotic pathways (Tuma and Hubbard, 2003;
301 Sandvig et al., 2018), caveolae are particularly abundant in vascular endothelial cells (Frank et
302 al., 2003). Caveolae are caveolin-coated 50-100 nm flask-shaped invaginations of the plasma
303 membrane (Palade, 1953; Palade, 1961). Furthermore, the suppression of caveolae-mediated
304 transcytosis regulates the development and function of both the mouse blood-retinal barrier and
305 the BBB (Andreone et al., 2017; Chow and Gu, 2017). Taken together, this suggests that the
306 increased transcytosis during early larval stages is most likely caveolae mediated. Interestingly,
307 the linear profile of Dextran uptake in the midbrain at 3 dpf closely resembles the caveolae-
308 mediated uptake of a fluorescently-conjugated aminopeptidase P (APP) antibody in the mouse
309 lung (Oh et al., 2007). While similarly linear, the scale is on the order of minutes in the larval
310 zebrafish brain versus seconds in the mouse lung. This discrepancy in timing is most likely due
311 to the large difference in the vesicular densities between the immature BBB endothelium (average
312 of 2 vesicles/μm^2) and the continuous endothelium of peripheral tissues, which ranges from 30 to
313 98 vesicles/μm^2 on the luminal membrane of diaphragm and myocardial endothelium (Simionescu
314 et al., 1974). Since loss of caveolin 1 is sufficient to precociously seal the blood-retinal barrier at
315 the angiogenic front (Chow and Gu, 2017), it would be interesting in future work to examine
316 whether zebrafish caveolin 1 mutants (Cao et al., 2016), which are viable as homozygotes, also
317 exhibit an earlier onset of BBB maturation.
318
319 BBB permeability is tightly regulated by endothelial cell interactions with pericytes and astroglial
320 cells. For the first time, we visualized their locations under TEM in zebrafish throughout barrier

321 development. Pericytes have been shown to be essential for establishing the mammalian BBB
322 (Armulik et al., 2010; Bell et al., 2010; Daneman et al., 2010). Similarly, pericyte deficient
323 notch3^{fh332} fish display increased BBB permeability in a tight junction independent manner like
324 pericyte-deficient mice (Wang et al., 2014). Our TEM data show that zebrafish pericytes are in
325 close contact with brain endothelial cells (Figures 2 and 5), even at the earliest stage examined
326 (3 dpf; Figure 2), and are embedded within the endothelial basement membrane as in mammals.
327 Our subcellular localization data is in line with a growing body of evidence for the conserved role
328 of pericytes in the zebrafish BBB (Wang et al., 2014; Lei et al., 2017). While zebrafish lack stellate
329 astrocytes, they possess radial glia that express several astrocytic markers, such as Gfap,
330 glutamine synthetase (GS), and Aqp4 (Jeong et al., 2008; Grupp et al., 2010). Previous studies
331 have disagreed on the extent of radial glia interactions with BBB endothelial cells in zebrafish.
332 Some studies report glia-BBB interactions that are similar to those observed in mammals (Jeong
333 et al., 2008), while others report little to no interaction (Grupp et al., 2010). Our TEM data in adult
334 zebrafish do not find a necessity for glial interactions with the brain vasculature, with endothelial
335 cells occasionally in contact with electron-light glia (Figure 5B), but often not (Figure 5A). This
336 appears to be a unique feature of the zebrafish BBB and should be considered carefully when
337 using zebrafish as a model system for the BBB.
338
339 Taken together this study provides a thorough characterization of the development of the
340 zebrafish BBB, highlighting regional differences in timing of maturation and capturing the
341 dynamics of the immature BBB. Furthermore, our developmental TEM series provides the first
342 direct evidence of vesicular trafficking regulating zebrafish BBB development. Finally, we have
343 shown that this down-regulation of vesicular trafficking is necessary for BBB formation, as
344 *mfsd2aa* mutants display increased barrier permeability due to unsuppressed transcytosis. We
345 hope that this work will serve as a launching pad for future studies using zebrafish to understand
346 the molecular regulators of BBB development and homeostasis in vertebrates.

347 **Author Contributions**

348 N.M.O., S.G.M. and C.G. conceived the project and designed experiments. N.M.O. performed all
349 experiments and analyzed all data. N.M.O., S.G.M. and C.G wrote the manuscript.

350

351 **Acknowledgments**

352 We thank members of the Gu and Megason laboratories for data discussion and comments on
353 the manuscript; Dr. Zach O'Brown for discussions and comments on the manuscript; Dr. Bela
354 Anand-Apte (Cleveland Clinic) for providing the transgenic *l-fabp:DBP-EGFP* fish line (Xie et al.,
355 2010) and Dr. Leonard Zon for providing the transgenic Tg(*kdrl:HRAS-mCherry*) line; and the
356 HMS Electron Microscopy Core Facility, with special thanks to Louise Trakimas for all of her
357 assistance in troubleshooting and preparing the TEM samples. This work was supported by the
358 Damon Runyon Cancer Foundation (N.M.O.), the Mahoney postdoctoral fellowship (N.M.O.), the
359 Fidelity Biosciences Research Initiative (C.G.), and the NIH DP1 NS092473 Pioneer Award
360 (C.G.). The research of C.G. was also supported in part by a Faculty Scholar grant from the
361 Howard Hughes Medical Institute.

362 **Materials and Methods**

363

364 **Zebrafish Strains and Maintenance**

365 Zebrafish were maintained at 28.5°C following standard protocols (Westerfield, 1993). All
366 zebrafish work was approved by the Harvard Medical Area Standing Committee on Animals under
367 protocol number 04487. Adult fish were maintained on a standard light-dark cycle from 9 am to
368 11 pm. Adult fish, age 3 months to 2 years, were crossed to produce embryos and larvae. These
369 studies used the AB wildtype strain and the transgenic strains Tg(*l-fabp:DBP-EGFP),*
370 Tg(*kdrl:mCherry*), and Tg(*kdrl:HRAS-mCherry*).

371

372 **Tracer Injections**

373 Larvae were immobilized with tricaine and placed in an agarose injection mold with their hearts
374 facing upwards. 2.3 nl of Alexa Fluor 405 NHS Ester (Thermo Fisher: A30000) or Alexa Fluor 647
375 10 kDa Dextran (Thermo Fisher:D22914) fluorescently conjugated tracers (10 mg/ml) were
376 injected into the cardiac sac using Nanoject II (Drummond Scientific, Broomall, PA). Embryos
377 were then mounted with 1.5% low gelling agarose (Sigma: A9414) in embryo water on 0.17 mm
378 coverslips and imaged live within 2 hours post injection. For developmental electron microscopy
379 experiments, 2.3 nl of 5 nm NHS-activated gold nanoparticles (Cytodiagnostics: CGN5K-5-1,
380 ~1.1^{14} particles/ml in PBS) were injected into the cardiac sac just as for the fluorescently
381 conjugated tracers. After 5 minutes of circulation, the fish were fixed for electron microscopy.
382 Adults were briefly immobilized with tricaine and retroorbitally injected with 3 µl of HRP (2 mg/ml
383 dissolved in PBS) using a 10 µl Hamilton syringe. After 30 minutes of HRP circulation, the brains
384 were fixed in 4% PFA overnight at 4C. Following fixation the brains were washed three times and
385 sectioned coronally with a vibratome (50 µm). Sections were then stained at room temperature in
386 0.05 M Tris-HCl pH 7.6 buffer containing 0.5 mg/ml 3-39 diaminobenzidine (DAB, Sigma Aldrich)
387 and 0.01% hydrogen peroxide.

388 **Transmission Electron Microscopy (TEM)**

389 Fish were anesthetized with tricaine and initially fixed by immersion in 4% paraformaldehyde
390 (VWR:15713-S) /0.1M sodium-cacodylate (VWR:11653). Following this initial fixation, the larval
391 fish and adults with exposed brains were further fixed for 7-14 days in 2% glutaraldehyde (Electron
392 Microscopy Sciences: 16320)/ 4% paraformaldehyde/ 0.1M sodium-cacodylate at room
393 temperature. Following fixation, larvae or dissected brains were washed overnight in 0.1M
394 sodium-cacodylate. Entire larval heads or coronal vibratome free-floating sections of adult brains
395 (50 µm) were post-fixed in 1% osmium tetroxide and 1.5% potassium ferrocyanide, dehydrated,
396 and embedded in epoxy resin. Ultrathin sections of 80 nm were then cut from the block surface
397 and collected on copper grids. The adult sections were counter-stained with Reynold's lead citrate
398 prior to imaging.

399

400 **CRISPR Mutants**

401 *Mfsd2aa* mutant fish were generated by injection of Cas9 RNA and a single guide RNA (5'-
402 GGTGTGTTTTGCGATCGGAG-3') targeting exon 3 into single-cell fertilized wildtype embryos.
403 *Mfsd2ab* mutant fish were generated by injection of Cas9 protein and a single guide RNA (5'-
404 TGAGAGCAGAGTAGGGCACG-3') targeting exon 5 into single-cell fertilized double transgenic
405 Tg(*l-fabp:DBP-EGFP; kdrl:mCherry)* embryos. F0 injected fish were raised, outcrossed to
406 wildtype fish and screened for potential mutant founders by PCR and sequencing. The stable
407 *mfsd2aa* mutant line was genotyped using 5'-AAATCACCTCTTCCAGTGAGGA-3' and 5'-
408 ATAGTAACAAAACGATGCTGAGCC-3' primers. *Mfsd2ab* mutants were genotyped using 5'-
409 GTCTACTCCATTTGCTGTACTTTGC-3' and 5'-CAGGTCAATCTCAGTGCTGATACAG-3'
410 primers.

411

412 **Imaging**

413 All live imaging of tracer permeability was performed on a Leica SP8 laser scanning confocal
414 microscope. Time lapse imaging was performed on the SP8 using a resonance scanner. A
415 1200EX electron microscope (JOEL) equipped with a 2k CCD digital camera (AMT) was used for
416 all TEM studies. Images were visualized and quantified using ImageJ (NIH) and Adobe
417 Photoshop. Time lapse videos were visualized as 3D reconstructions and cropped to highlight
418 particular blood vessels of interest using Imaris software (Bitplane).

419

420 **Tracer Permeability Quantification**

421 All quantification was performed on blinded image sets. Parenchymal cells containing injected
422 tracers outside of the blood vessels were manually counted throughout z-stacks that spanned the
423 entire larval brain in depth. Z-stacks were collected with 0.59 μm z-steps using a 25x water
424 immersion objective on a Leica SP8 laser scanning confocal microscope. The Dextran intensity
425 was measured in six parenchymal regions of average intensity projections of the time lapse videos
426 and averaged as a single value per fish. These values were normalized to the average
427 fluorescence intensity in the lumen at each time point.

428

429 **TEM Quantification**

430 For all TEM quantifications, vesicular density values were calculated from the number of non-
431 clathrin coated flask-shaped vesicles per μm of endothelial luminal or abluminal membrane for
432 each image collected. Embryonic basement membrane gold intensity was measured in three
433 regions per endothelial cell and normalized to luminal gold intensity values within individual
434 images using ImageJ. All images for analysis were collected at 12000x magnification on the JOEL
435 1200EX electron microscope. 10-15 vessels were quantified for each fish, with each color
436 representing a different fish.

437

438 **Statistical Analysis**

439 All statistical analyses were performed using Prism 8 (GraphPad Software). Two group
440 comparisons were analyzed using an unpaired two-tailed t test. Nested t tests were employed for
441 all electron microscopy comparisons to account for the actual N versus vessels analyzed. Multiple
442 group comparisons were analyzed with one-way ANOVA, followed by a post hoc Tukey's multiple
443 comparison test. The time lapse leakage dynamics were analyzed with a Mann-Whitney U test to
444 discriminate whether the two patterns of leakage accumulation were different. Sample size for all
445 experiments was determined empirically using standards generally employed by the field, and no
446 data was excluded when performing statistical analysis. Standard error of the mean was
447 calculated for all experiments and displayed as errors bars in graphs. Statistical details for specific
448 experiments, including exact n values and what n represents, precision measures, statistical tests
449 used, and definitions of significance can be found in the Figure Legends.

450

451 Ablain, J., Durand, E.M., Yang, S., Zhou, Y., and Zon, L.I. 2015. A CRISPR/Cas9 Vector System
452 for Tissue-Specific Gene Disruption in Zebrafish. Dev. Cell **32**(6): 756–764. Elsevier Inc.
453 doi:10.1016/j.devcel.2015.01.032.
454 Albadri, S., Del Bene, F., and Revenu, C. 2017. Genome editing using CRISPR/Cas9-based
455 knock-in approaches in zebrafish. Methods **121-122**: 77–85. Elsevier Inc.
456 doi:10.1016/j.ymeth.2017.03.005.
457 Andreone, B.J., Chow, B.W., Tata, A., Lacoste, B., Ben-Zvi, A., Bullock, K., Deik, A.A., Ginty,
458 D.D., Clish, C.B., and Gu, C. 2017. Blood-Brain Barrier Permeability Is Regulated by Lipid
459 Transport-Dependent Suppression of Caveolae-Mediated Transcytosis. Neuron **94**(3): 581–
460 594.e5. doi:10.1016/j.neuron.2017.03.043.
461 Andreone, B.J., Lacoste, B., and Gu, C. 2015. Neuronal and Vascular Interactions.
462 http://dx.doi.org.ezp-prod1.hul.harvard.edu/10.1146/annurev-neuro-071714-033835. Annual
463 Reviews. doi:10.1146/annurev-neuro-071714-033835.
464 Armer, H.E.J., Mariggi, G., Png, K.M.Y., Genoud, C., Monteith, A.G., Bushby, A.J., Gerhardt, H.,
465 and Collinson, L.M. 2009. Imaging Transient Blood Vessel Fusion Events in Zebrafish by
466 Correlative Volume Electron Microscopy. PLoS ONE **4**(11): e7716–10.
467 doi:10.1371/journal.pone.0007716.
468 Armulik, A., Genové, G., Mäe, M., Nisancioglu, M.H., Wallgard, E., Niaudet, C., He, L., Norlin, J.,
469 Lindblom, P., Strittmatter, K., Johansson, B.R., and Betsholtz, C. 2010. Pericytes regulate the
470 blood-brain barrier. Nature **468**(7323): 557–561. doi:10.1038/nature09522.
471 Bell, R.D., Winkler, E.A., Sagare, A.P., Singh, I., LaRue, B., Deane, R., and Zlokovic, B.V. 2010b.
472 Pericytes control key neurovascular functions and neuronal phenotype in the adult brain and
473 during brain aging. Neuron **68**(3): 409–427. doi:10.1016/j.neuron.2010.09.043.
474 Ben-Zvi, A., Lacoste, B., Kur, E., Andreone, B.J., Mayshar, Y., Yan, H., and Gu, C. 2014. Mfsd2a
475 is critical for the formation and function of the blood-brain barrier. Nature **509**(7501): 507–
476 511. doi:10.1038/nature13324.
477 Brightman, M.W., and Reese, T.S. 1969. Junctions between intimately apposed cell membranes
478 in the vertebrate brain. J. Cell Biol. **40**(3): 648–677.
479 Campbell, M., Kiang, A.-S., Kenna, P.F., Kerskens, C., Blau, C., O'Dwyer, L., Tivnan, A., Kelly,
480 J.A., Brankin, B., Farrar, G.-J., and Humphries, P. 2008. RNAi-mediated reversible opening
481 of the blood-brain barrier. J. Gene Med. **10**(8): 930–947. doi:10.1002/jgm.1211.
482 Cao, J., Navis, A., Ben D Cox, Dickson, A.L., Gemberling, M., Karra, R., Bagnat, M., and Poss,
483 K.D. 2016. Single epicardial cell transcriptome sequencing identifies Caveolin 1 as an
484 essential factor in zebrafish heart regeneration. Development **143**(2): 232–243. Oxford
485 University Press for The Company of Biologists Limited. doi:10.1242/dev.130534.
486 Chow, B.W., and Gu, C. 2017. Gradual Suppression of Transcytosis Governs Functional Blood-
487 Retinal Barrier Formation. Neuron **93**(6): 1325–1333.e3. Elsevier Inc.
488 doi:10.1016/j.neuron.2017.02.043.
489 Daneman, R., Zhou, L., Kebede, A.A., and Barres, B.A. 2010. Pericytes are required for blood-
490 brain barrier integrity during embryogenesis. Nature **468**(7323): 562–566.
491 doi:10.1038/nature09513.
492 Fleming, A., Diekmann, H., and Goldsmith, P. 2013. Functional characterisation of the maturation
493 of the blood-brain barrier in larval zebrafish. PLoS ONE **8**(10): e77548.
494 doi:10.1371/journal.pone.0077548.
495 Franco, C.A., Jones, M.L., Bernabeu, M.O., Geudens, I., Mathivet, T., Rosa, A., Lopes, F.M.,
496 Lima, A.P., Ragab, A., Collins, R.T., Phng, L.-K., Coveney, P.V., and Gerhardt, H. 2015.
497 Dynamic Endothelial Cell Rearrangements Drive Developmental Vessel Regression. PLoS
498 Biol. **13**(4): e1002125–19. doi:10.1371/journal.pbio.1002125.
499 Frank, P.G., Woodman, S.E., Park, D.S., and Lisanti, M.P. 2003. Caveolin, Caveolae, and
500 Endothelial Cell Function. Arterioscler. Thromb. Vasc. Biol. **23**(7): 1161–1168.
501 doi:10.1161/01.ATV.0000070546.16946.3A.

502 Gagnon, J.A., Valen, E., Thyme, S.B., Huang, P., Ahkmetova, L., Pauli, A., Montague, T.G.,
503 Zimmerman, S., Richter, C., and Schier, A.F. 2014. Efficient Mutagenesis by Cas9 Protein-
504 Mediated Oligonucleotide Insertion and Large-Scale Assessment of Single-Guide RNAs.
505 PLoS ONE **9**(5): e98186–8. doi:10.1371/journal.pone.0098186.
506 Galanternik, M.V., Castranova, D., Gore, A.V., Blewett, N.H., Jung, H.M., Stratman, A.N., Kirby,
507 M.R., Iben, J., Miller, M.F., Kawakami, K., Maraia, R.J., and Weinstein, B.M. 2017. A novel
508 perivascular cell population in the zebrafish brain. Elife **6**: 45. doi:10.7554/eLife.24369.
509 Geudens, I., Coxam, B., Alt, S., Gebala, V., Vion, A.-C., Rosa, A., and Gerhardt, H. 2018. Arterio-
510 Venous Remodeling in the Zebrafish Trunk Is Controlled by Genetic Programming and Flow-
511 Mediated Fine-Tuning. : 1–32. doi:10.1101/403550.
512 Geudens, I., Herpers, R., Hermans, K., Segura, I., Ruiz de Almodovar, C., Bussmann, J., De
513 Smet, F., Vandevelde, W., Hogan, B.M., Siekmann, A., Claes, F., Moore, J.C., Pistocchi, A.S.,
514 Loges, S., Mazzone, M., Mariggi, G., Bruyère, F., Cotelli, F., Kerjaschki, D., Noël, A., Foidart,
515 J.-M., Gerhardt, H., Ny, A., Langenberg, T., Lawson, N.D., Duckers, H.J., Schulte-Merker, S.,
516 Carmeliet, P., and Dewerchin, M. 2010. Role of Delta-like-4/Notch in the Formation and
517 Wiring of the Lymphatic Network in Zebrafish. Arterioscler. Thromb. Vasc. Biol. **30**(9): 1695–
518 1702. doi:10.1161/ATVBAHA.110.203034.
519 Grupp, L., Wolburg, H., and Mack, A.F. 2010. Astroglial structures in the zebrafish brain. Journal
520 of Comparative Neurology **518**(21): 4277–4287. Wiley Subscription Services, Inc., A Wiley
521 Company. doi:10.1002/cne.22481.
522 Guemez-Gamboa, A., Nguyen, L.N., Yang, H., Zaki, M.S., Kara, M., Ben-Omran, T., Akizu, N.,
523 Rosti, R.O., Rosti, B., Scott, E., Schroth, J., Copeland, B., Vaux, K.K., Cazenave-Gassiot, A.,
524 Quek, D.Q.Y., Wong, B.H., Tan, B.C., Wenk, M.R., Gunel, M., Gabriel, S., Chi, N.C., Silver,
525 D.L., and Gleeson, J.G. 2015. Inactivating mutations in MFSD2A, required for omega-3 fatty
526 acid transport in brain, cause a lethal microcephaly syndrome. Nat. Genet. **47**(7): 809–813.
527 doi:10.1038/ng.3311.
528 Harel, T., Quek, D.Q.Y., Wong, B.H., Cazenave-Gassiot, A., Wenk, M.R., Fan, H., Berger, I.,
529 Shmueli, D., Shaag, A., Silver, D.L., Elpeleg, O., and Edvardson, S. 2018. Homozygous
530 mutation in MFSD2A, encoding a lysolipid transporter for docosahexanoic acid, is associated
531 with microcephaly and hypomyelination. Neurogenetics **19**(4): 227-235. doi:10.1007/s10048-
532 018-0556-6.
533 Herbert, S.P., Cheung, J.Y.M., and Stainier, D.Y.R. 2012. Determination of Endothelial Stalk
534 versus Tip Cell Potential during Angiogenesis by H2.0-like Homeobox-1. Current Biology
535 **22**(19): 1789–1794. Elsevier Ltd. doi:10.1016/j.cub.2012.07.037.
536 Herbert, S.P., Huisken, J., Kim, T.N., Feldman, M.E., Houseman, B.T., Wang, R.A., Shokat, K.M.,
537 and Stainier, D.Y.R. 2009. Arterial-venous segregation by selective cell sprouting: an
538 alternative mode of blood vessel formation. Science **326**(5950): 294–298.
539 doi:10.1126/science.1178577.
540 Hogan, B.M., and Schulte-Merker, S. 2017. How to Plumb a Pisces: Understanding Vascular
541 Development and Disease Using Zebrafish Embryos. Dev. Cell **42**(6): 567–583. Elsevier.
542 doi:10.1016/j.devcel.2017.08.015.
543 Hwang, W.Y., Fu, Y., Reyon, D., Maeder, M.L., Tsai, S.Q., Sander, J.D., Peterson, R.T., Yeh, J.-
544 R.J., and Joung, J.K. 2013. Efficient genome editing in zebrafish using a CRISPR-Cas
545 system. Nat. Biotechnol. **31**(3): 227–229. doi:10.1038/nbt.2501.
546 Janzer, R.C., and Raff, M.C. 1987. Astrocytes induce blood-brain barrier properties in endothelial
547 cells. Nature **325**(6101): 253–257. doi:10.1038/325253a0.
548 Jin, S.-W., Beis, D., Mitchell, T., Chen, J.-N., and Stainier, D.Y.R. 2005. Cellular and molecular
549 analyses of vascular tube and lumen formation in zebrafish. Development **132**(23): 5199–
550 5209. The Company of Biologists Ltd. doi:10.1242/dev.02087.

551 Jeong, J.-Y., Kwon, H.-B., Ahn, J.-C., Kang, D., Kwon, S.-H., Park, J.A., and Kim, K.-W. 2008.
552 Functional and developmental analysis of the blood–brain barrier in zebrafish. Brain Res.
553 Bull. **75**(5): 619–628. doi:10.1016/j.brainresbull.2007.10.043.
554 Lawson, N.D., and Weinstein, B.M. 2002. In Vivo Imaging of Embryonic Vascular Development
555 Using Transgenic Zebrafish. Dev. Biol. **248**(2): 307–318. doi:10.1006/dbio.2002.0711.
556 Lei, D., Jin, X., Wen, L., Dai, H., Ye, Z., and Wang, G. 2017. bmp3 is Required for Integrity of
557 Blood Brain Barrier by Promoting Pericyte Coverage in Zebrafish Embryos. *Current Molecular*
558 *Medicine*, *17*(4).
559 Matsuoka, R.L., Marass, M., Avdesh, A., Helker, C.S., Maischein, H.-M., Grosse, A.S., Kaur, H.,
560 Lawson, N.D., Herzog, W., and Stainier, D.Y. 2016. Radial glia regulate vascular patterning
561 around the developing spinal cord. Elife **5**: 1328. doi:10.7554/eLife.20253.
562 Nitta, T., Hata, M., Gotoh, S., Seo, Y., Sasaki, H., Hashimoto, N., Furuse, M., and Tsukita, S.
563 2003. Size-selective loosening of the blood-brain barrier in claudin-5-deficient mice. J. Cell
564 Biol. **161**(3): 653–660. Rockefeller University Press. doi:10.1083/jcb.200302070.
565 O'Brown, N.M., Pfau, S.J., and Gu, C. 2018. Bridging barriers: a comparative look at the blood–
566 brain barrier across organisms. **32**(7-8): 466–478. doi:10.1101/gad.309823.117.
567 Oh, P., Borgström, P., Witkiewicz, H., Li, Y., Borgström, B.J., Chrastina, A., Iwata, K., Zinn, K.R.,
568 Baldwin, R., Testa, J.E., and Schnitzer, J.E. 2007. Live dynamic imaging of caveolae pumping
569 targeted antibody rapidly and specifically across endothelium in the lung. Nat. Biotechnol.
570 **25**(3): 327–337. doi:10.1038/nbt1292.
571 Palade, G.E. 1953. Fine structure of blood capillaries. J. Appl. Phys. **24**: 1424.
572 Palade, G.E. 1961. Blood capillaries of the heart and other organs. Circulation **24**: 368–388.
573 Phng, L.-K., Potente, M., Leslie, J.D., Babbage, J., Nyqvist, D., Lobov, I., Ondr, J.K., Rao, S.,
574 Lang, R.A., Thurston, G., and Gerhardt, H. 2009. Nrarp Coordinates Endothelial Notch and
575 Wnt Signaling to Control Vessel Density in Angiogenesis. Dev. Cell **16**(1): 70–82. Elsevier.
576 doi:10.1016/j.devcel.2008.12.009.
577 Quiñonez-Silvero, C., Hübner, K., and Herzog, W. 2019. Development of the brain vasculature
578 and the blood-brain barrier in zebrafish. Dev. Biol.: 1–34. Elsevier Inc.
579 doi:10.1016/j.ydbio.2019.03.005.
580 Reese, T.S., and Karnovsky, M.J. 1967. Fine structural localization of a blood-brain barrier to
581 exogenous peroxidase. J. Cell Biol. **34**(1): 207–217. The Rockefeller University Press.
582 Sanchez-Covarrubias, L., Slosky, L.M., Thompson, B.J., Davis, T.P., and Ronaldson, P.T. 2014.
583 Transporters at CNS barrier sites: obstacles or opportunities for drug delivery? Curr. Pharm.
584 Des. **20**(10): 1422–1449.
585 Sandvig, K., Kavaliauskiene, S., and Skotland, T. 2018. Clathrin-independent endocytosis: an
586 increasing degree of complexity. Histochem. Cell Biol. **150**(2): 107–118. doi:10.1007/s00418-
587 018-1678-5.
588 Santoro, M.M., Samuel, T., Mitchell, T., Reed, J.C., and Stainier, D.Y.R. 2007. Birc2 (cIap1)
589 regulates endothelial cell integrity and blood vessel homeostasis. Nat. Genet. **39**(11): 1397–
590 1402. doi:10.1038/ng.2007.8.
591 Simionescu, M., Simionescu, N., and Palade, G.E. 1974. Morphometric data on the endothelium
592 of blood capillaries. J. Cell Biol. **60**(1): 128–152. Rockefeller University Press.
593 doi:10.1083/jcb.60.1.128.
594 Sohet, F., Lin, C., Munji, R.N., Lee, S.Y., Ruderisch, N., Soung, A., Arnold, T.D., Derugin, N.,
595 Vexler, Z.S., Yen, F.T., and Daneman, R. 2015. LSR/angulin-1 is a tricellular tight junction
596 protein involved in blood-brain barrier formation. J. Cell Biol. **208**(6): 703–711. Rockefeller
597 University Press. doi:10.1083/jcb.201410131.
598 Stratman, A.N., Pezoa, S.A., Farrelly, O.M., Castranova, D., Dye, L.E., III, Butler, M.G., Sidik, H.,
599 Talbot, W.S., and Weinstein, B.M. 2017. Interactions between mural cells and endothelial
600 cells stabilize the developing zebrafish dorsal aorta. Development **144**(1): 115–127.
601 doi:10.1242/dev.143131.

602 Stewart, P.A., and Wiley, M.J. 1981. Developing nervous tissue induces formation of blood-brain
603 barrier characteristics in invading endothelial cells: a study using quail--chick transplantation
604 chimeras. Dev. Biol. **84**(1): 183–192.
605 Tuma, P.L., and Hubbard, A.L. 2003. Transcytosis: Crossing Cellular Barriers. Physiological
606 Reviews **83**(3): 871–932. doi:10.1152/physrev.00001.2003.
607 Ulrich, F., Carretero-Ortega, J., Menéndez, J., Narvaez, C., Sun, B., Lancaster, E., Pershad, V.,
608 Trzaska, S., Véliz, E., Kamei, M., Prendergast, A., Kidd, K.R., Shaw, K.M., Castranova, D.A.,
609 Pham, V.N., Lo, B.D., Martin, B.L., Raible, D.W., Weinstein, B.M., and Torres-Vázquez, J.
610 2016. Reck enables cerebrovascular development by promoting canonical Wnt signaling.
611 Development **143**(1): 147–159. doi:10.1242/dev.123059
612 Umans, R.A., Henson, H.E., Mu, F., Parupalli, C., Ju, B., Peters, J.L., Lanham, K.A., Plavicki,
613 J.S., and Taylor, M.R. 2017. CNS angiogenesis and barriergenesis occur simultaneously.
614 Dev. Biol. **425**(2): 101–108. doi:10.1016/j.ydbio.2017.03.017.
615 Vanhollebeke, B., Stone, O.A., Bostaille, N., Cho, C., Zhou, Y., Maquet, E., Gauquier, A.,
616 Cabochette, P., Fukuhara, S., Mochizuki, N., Nathans, J., and Stainier, D.Y. 2015. Tip cell-
617 specific requirement for an atypical Gpr124- and Reck-dependent Wnt/β-catenin pathway
618 during brain angiogenesis. Elife **4**. doi:10.7554/eLife.06489.
619 Varshney, G.K., Sood, R., and Burgess, S.M. 2015. Understanding and Editing the Zebrafish
620 Genome. *In* Advances in Genetics. Elsevier Ltd. doi:10.1016/bs.adgen.2015.09.002.
621 Wang, Y., Pan, L., Moens, C.B., and Appel, B. 2014. Notch3 establishes brain vascular integrity
622 by regulating pericyte number. Development **141**(2): 307–317. Oxford University Press for
623 The Company of Biologists Limited. doi:10.1242/dev.096107.
624 Westerfield, M. 1993. The zebrafish book: a guide for the laboratory use of zebrafish (Brachydanio
625 rerio).
626 Wilkinson, R.N., and van Eeden, F.J.M. 2014. The Zebrafish as a Model of Vascular Development
627 and Disease. *In* Genetics of Cardiovascular Disease, 1st edition. Elsevier Inc.
628 doi:10.1016/B978-0-12-386930-2.00005-7.
629 Xie, J., Farage, E., Sugimoto, M., and Anand-Apte, B. 2010. A novel transgenic zebrafish model
630 for blood-brain and blood-retinal barrier development. BMC Dev. Biol. **10**: 76.
631 doi:10.1186/1471-213X-10-76.
632 Yanagida, K., Liu, C.H., Faraco, G., Galvani, S., Smith, H.K., Burg, N., Anrather, J., Sanchez, T.,
633 Iadecola, C., and Hla, T. 2017. Size-selective opening of the blood–brain barrier by targeting
634 endothelial sphingosine 1–phosphate receptor 1. Proc. Natl. Acad. Sci. U.S.A. **114**(17):
635 4531–4536. doi:10.1073/pnas.1618659114.
636 Zhao, Z., Nelson, A.R., Betsholtz, C., and Zlokovic, B.V. 2015. Establishment and Dysfunction of
637 the Blood-Brain Barrier. Cell **163**(5): 1064–1078. doi:10.1016/j.cell.2015.10.067.

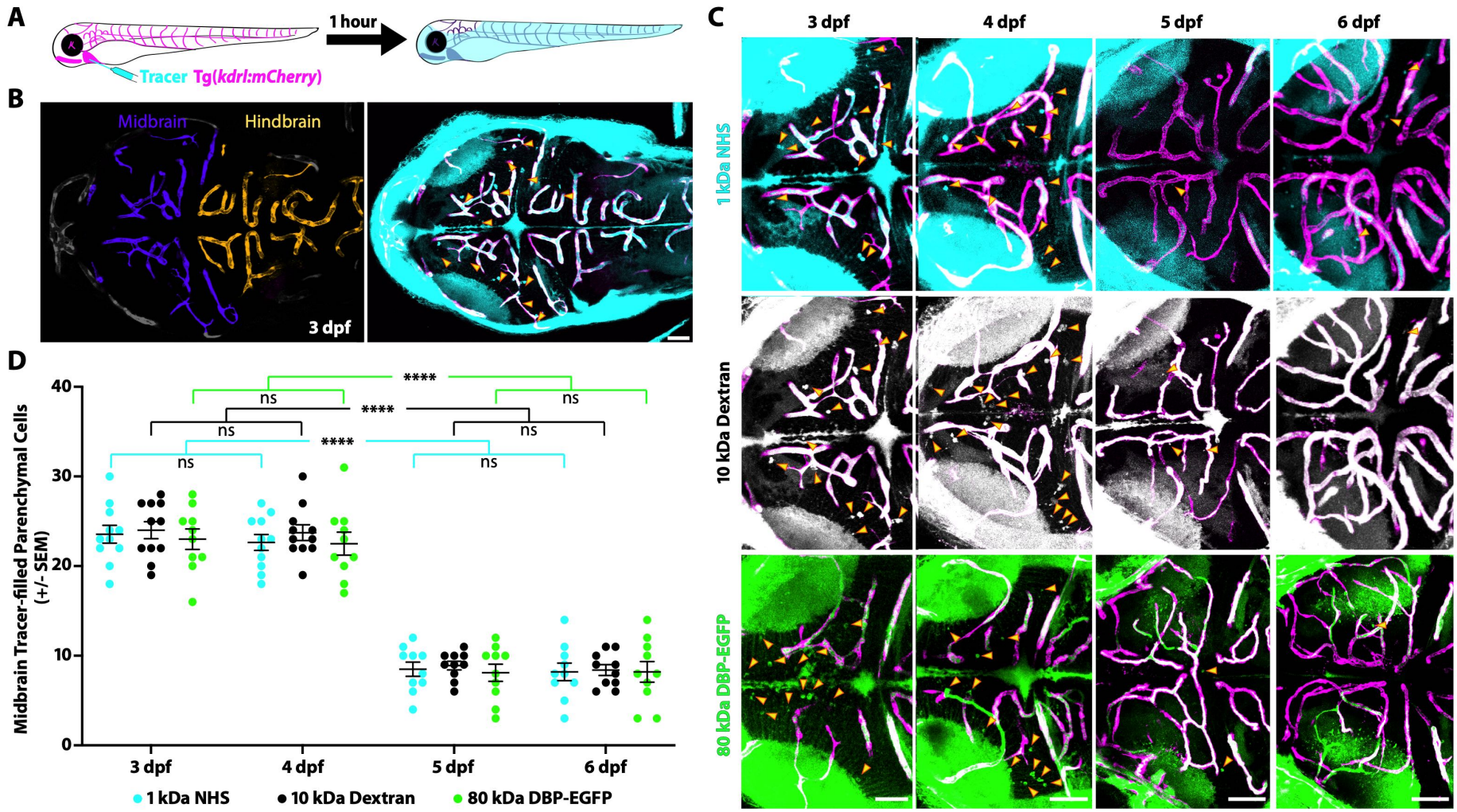
A
1 hour
Tracer
Tg(kdrl:mCherry)
B
Midbrain
Hindbrain
3 dpf
C
3 dpf
4 dpf
5 dpf
6 dpf
1 kDa NHS
10 kDa Dextran
80 kDa DBP-EGFP
D
Midbrain Tracer-filled Parenchymal Cells (+/- SEM)
40
30
20
10
0
****
ns
3 dpf
4 dpf
5 dpf
6 dpf
1 kDa NHS
10 kDa Dextran
80 kDa DBP-EGFP

639 **Figure 1. The midbrain BBB becomes functional at 5 dpf.** (A) Diagram of the tracer leakage
640 assay. Fluorescently conjugated tracers (turquoise) were injected intracardially into transgenic
641 fish that express mCherry in the vasculature (magenta; Tg(*kdrl:mCherry*)) and allowed to circulate
642 for one hour before imaging. (B) Dorsal view maximum intensity projection of the larval brain
643 vasculature at 3 dpf. Left image is pseudo-colored to demarcate the midbrain (violet) and the
644 hindbrain (gold) vasculature. Right image shows the NHS tracer (turquoise) in the entire larval
645 brain, with a large number of tracer-filled parenchymal cells marked by yellow arrowheads in the
646 midbrain. (C) Representative dorsal view maximum intensity projections of larval zebrafish
647 midbrains at different developmental stages reveal increased permeability at 3 and 4 dpf
648 compared to 5 and 6 dpf. The increased early permeability was observed with two injected tracers
649 of different sizes, a 1 kDa NHS (turquoise) and a 10 kDa Dextran (white), as well with an 80 kDa
650 transgenic serum protein DBP-EGFP (green). Yellow arrowheads demarcate the tracer-filled
651 parenchymal cells outside of the vasculature (magenta). Scale bars represent 50 μm. (D)
652 Quantification of tracer-filled parenchymal cells in the midbrain between 3 and 6 dpf reveals a
653 significant decrease in tracer uptake at 5 dpf. There was no difference in the number of
654 parenchymal cells that picked up the different tracers at any time point. There was no significant
655 change from 3 to 4 dpf or from 5 to 6 dpf, suggesting that the barrier seals around 5 dpf. N = 10-
656 11 fish, each represented as a single dot on the plot. The mean and the standard error are drawn
657 in black for each tracer and stage. **** $p<0.0001$, ns is not significant.

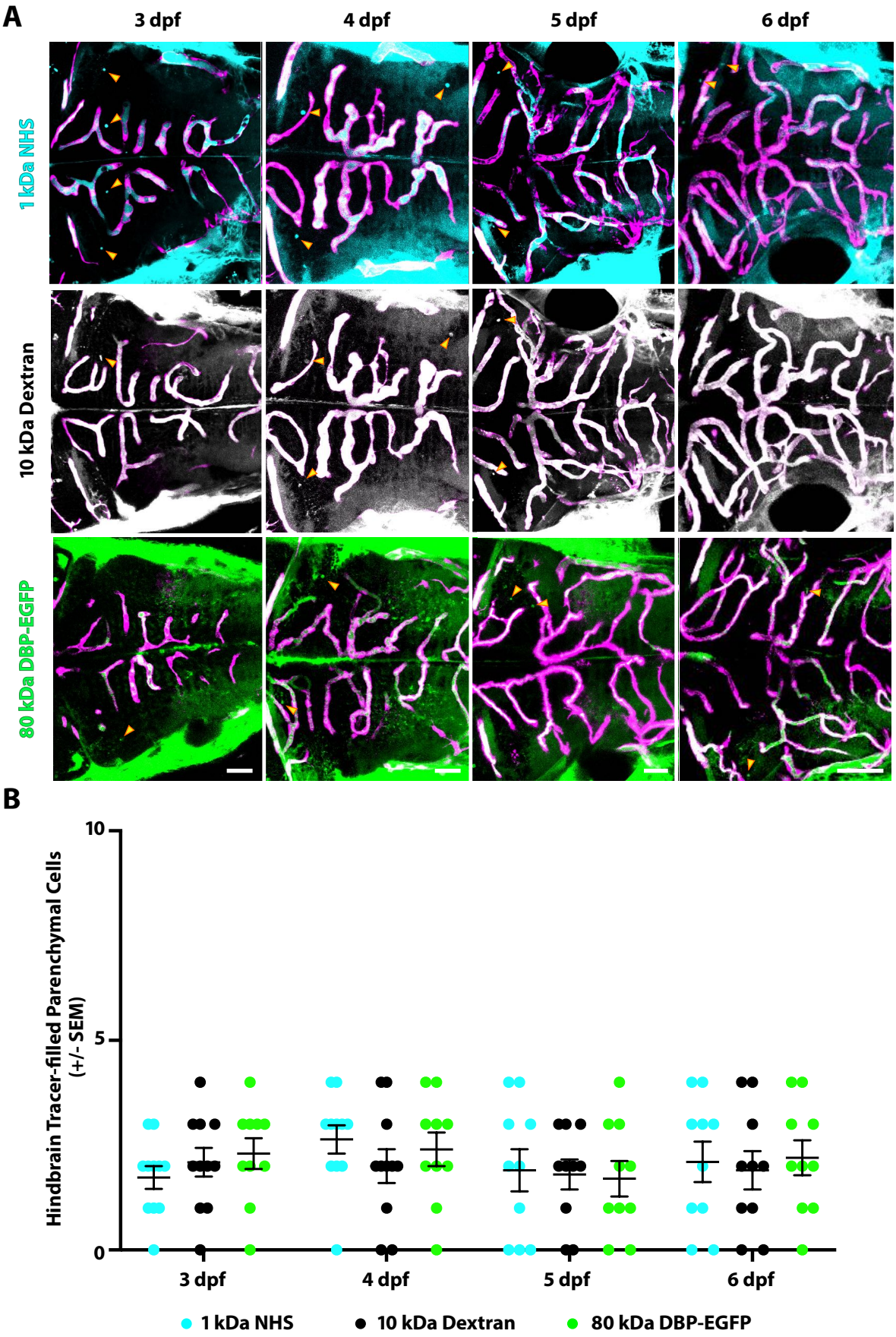
A
3 dpf
4 dpf
5 dpf
6 dpf
1 kDa NHS
10 kDa Dextran
80 kDa DBP-EGFP
B
Hindbrain Tracer-filled Parenchymal Cells (+/- SEM)
10
5
0
3 dpf
4 dpf
5 dpf
6 dpf
1 kDa NHS
10 kDa Dextran
80 kDa DBP-EGFP

658

659 **Figure 1 – Supplement 1. The hindbrain has a functional BBB at 3 dpf.** (A) Representative
660 dorsal view maximum intensity projections of larval zebrafish hindbrains at different
661 developmental stages reveals low permeability at 3 dpf that stays constant until 6 dpf. This low
662 permeability was observed with two injected tracers of different sizes, a 1 kDa NHS (turquoise)
663 and a 10 kDa Dextran (white), as well with an 80 kDa transgenic serum protein DBP-EGFP
664 (green). Yellow arrowheads demarcate the few tracer-filled parenchymal cells outside of the
665 vasculature (magenta). Scale bars represent 50 μm. (B) Quantification of tracer-filled
666 parenchymal cells in the hindbrain between 3 and 6 dpf reveals low tracer uptake beginning at 3
667 dpf. There was no difference in the number of parenchymal cells that picked up the different
668 tracers at any time point. N = 10-11 fish, each represented as a single dot on the plot. The mean
669 and the standard error are drawn in black for each tracer and stage.

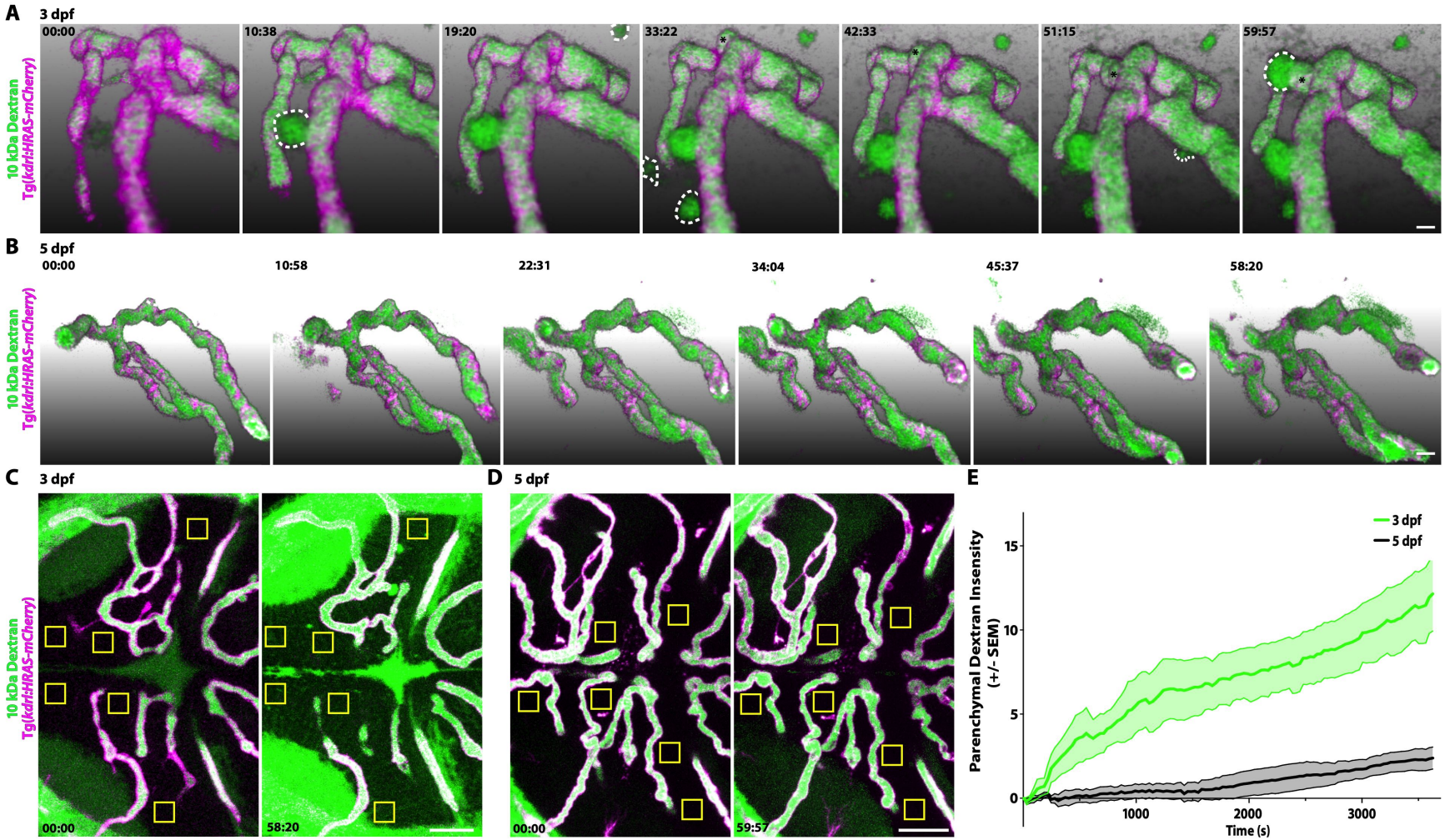
A
3 dpf
00:00
10:38
19:20
33:22
42:33
51:15
59:57
10 kDa Dextran
Tg(kdrl:HRAS-mCherry)
B
5 dpf
00:00
10:58
22:31
34:04
45:37
58:20
10 kDa Dextran
Tg(kdrl:HRAS-mCherry)
C
3 dpf
10 kDa Dextran
Tg(kdrl:HRAS-mCherry)
00:00
58:20
D
5 dpf
00:00
59:57
E
3 dpf
5 dpf
Parenchymal Dextran Insensity
(+/- SEM)
15
10
5
0
1000
2000
3000
Time (s)

671 **Figure 2. Dynamic tracer leakage in the developing BBB via live imaging.** (A) Time course
672 stills from Video 1 of tracer leakage at 3 dpf reveal an increase in parenchymal cells absorbing
673 the Dextran tracer (outlined by dashed white lines) as well as a general increase in overall Dextran
674 (green) intensity outside of the vasculature (magenta). An angiogenic tip cell becomes apparent
675 at 33:23 and is demarcated by an asterisk (*). This tip cell produces two separate bursts of
676 leakage observed in Video 2. (B) Time course stills of Dextran tracer dynamics at 5 dpf reveals a
677 mature BBB, with reduced overall Dextran extravasation into the brain parenchyma. The scale
678 bars represent 10 μm. (C and D) Dorsal maximum intensity projection of the midbrain at 3 dpf (C)
679 and 5 dpf (D) at the first and last time point examined. While there is a large increase in overall
680 parenchymal Dextran intensity over time at 3 dpf, the 5 dpf midbrain parenchyma appears
681 relatively unaltered after an hour of Dextran circulation. Boxed regions are representative of the
682 six areas per fish used for analysis in E. The scale bars represent 50 μm. (E) Quantification of
683 Dextran intensity in the brain parenchyma over time at 3 dpf (green) and 5 dpf (black) shows a
684 significant difference in tracer leakage dynamics ($p<0.0001$, Mann Whitney U test), with both more
685 total Dextran accumulation and a faster rate of Dextran accumulation in the brain parenchyma at
686 3 dpf. N=6 fish with 6 regions analyzed per fish.

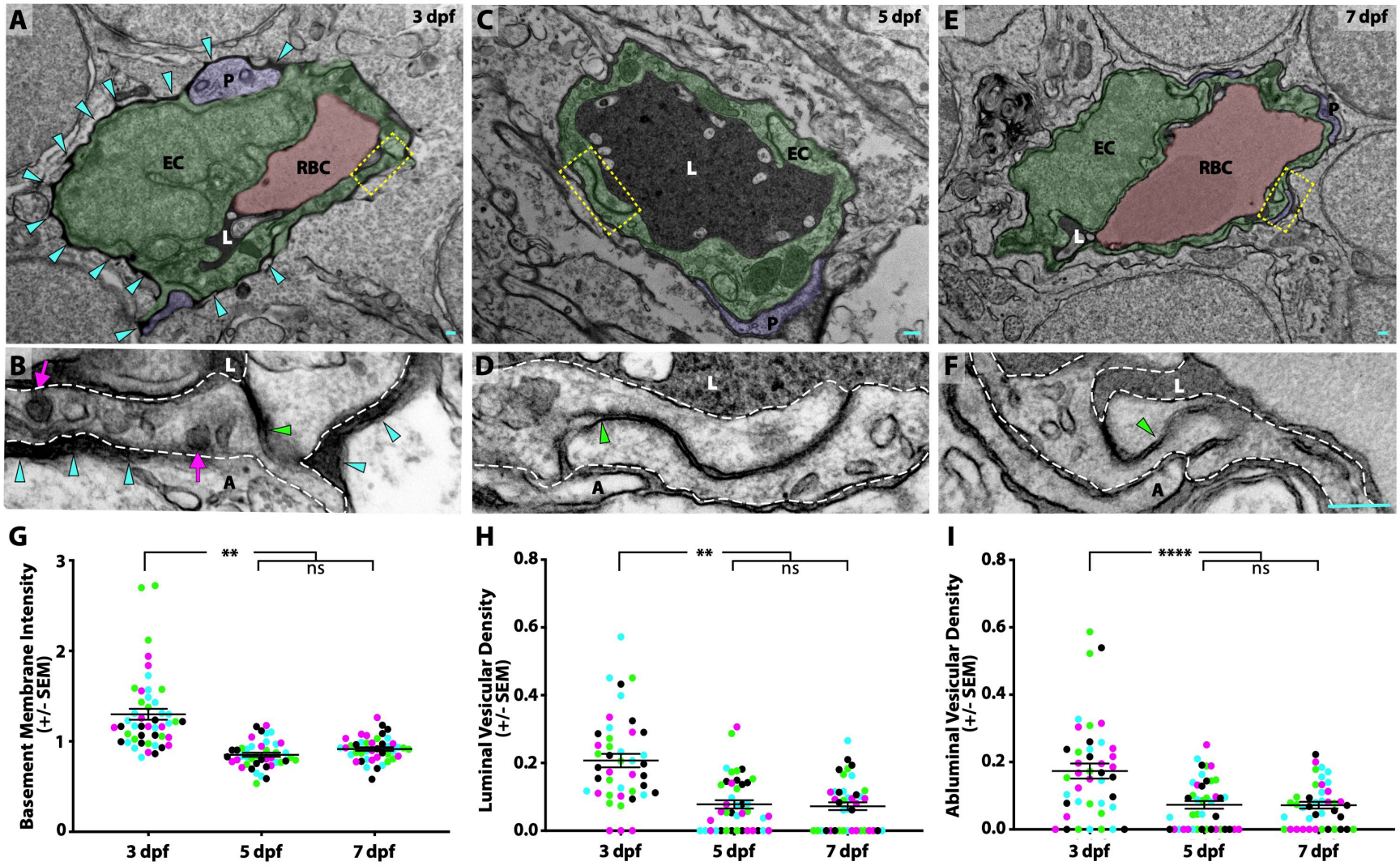
A
3 dpf
P
EC
RBC
L
B
L
A
C
5 dpf
L
EC
P
D
L
A
E
7 dpf
P
EC
RBC
L
F
L
A
G
Basement Membrane Intensity (+/- SEM)
**
ns
3 dpf
5 dpf
7 dpf
H
Luminal Vesicular Density (+/- SEM)
**
ns
3 dpf
5 dpf
7 dpf
I
Abluminal Vesicular Density (+/- SEM)
****
ns
3 dpf
5 dpf
7 dpf

688 **Figure 3. Suppression of transcytosis determines the timing of functional BBB formation.**
689 (A, C, E) TEM images of individual blood vessel cross-sections after injection of electron-dense
690 gold nanoparticles at 3 dpf (A), 5 dpf (C), and 7 dpf (E). Endothelial cells (EC) are pseudo-colored
691 green, pericytes (P) are pseudo-colored purple and red blood cells (RBC) are pseudo-colored red
692 when present in the lumen (L). Turquoise arrowheads highlight the gold-filled basement
693 membrane at 3 dpf (A). (B, D, F) High magnification images (25000x) of the areas boxed in A, C,
694 and E, respectively, with the endothelial cells outlined with white dashed lines. The images are
695 oriented with the lumen (L) on top and the ablumen (A) on the bottom. Tight junctions are
696 functional as early as 3 dpf (B), as seen by their ability to halt the gold nanoparticles at the so-
697 called "kissing point" (green arrowhead), and remain functional throughout development (D and
698 F). Even though the tight junctions are functional at 3 dpf, the endothelial basement membrane is
699 filled with electron-dense gold nanoparticles (B, turquoise arrowheads). This appears to be due
700 to an elevated level of luminal and abluminal gold-filled vesicles (magenta arrows). The scale bars
701 represent 200 nm. (G) Quantification of the endothelial basement membrane gold intensity
702 normalized to luminal gold intensity. (H and I) Quantification of the vesicular densities both on
703 the luminal (H) and abluminal (I) membrane of endothelial cells reveals a suppression of vesicular
704 densities beginning at 5 dpf that remains constant at 7 dpf. N=4 fish, each marked with a different
705 color, with at least 10 blood vessels quantified for each fish. **** $p<0.0001$, ** $p<0.01$, ns is not
706 significant.

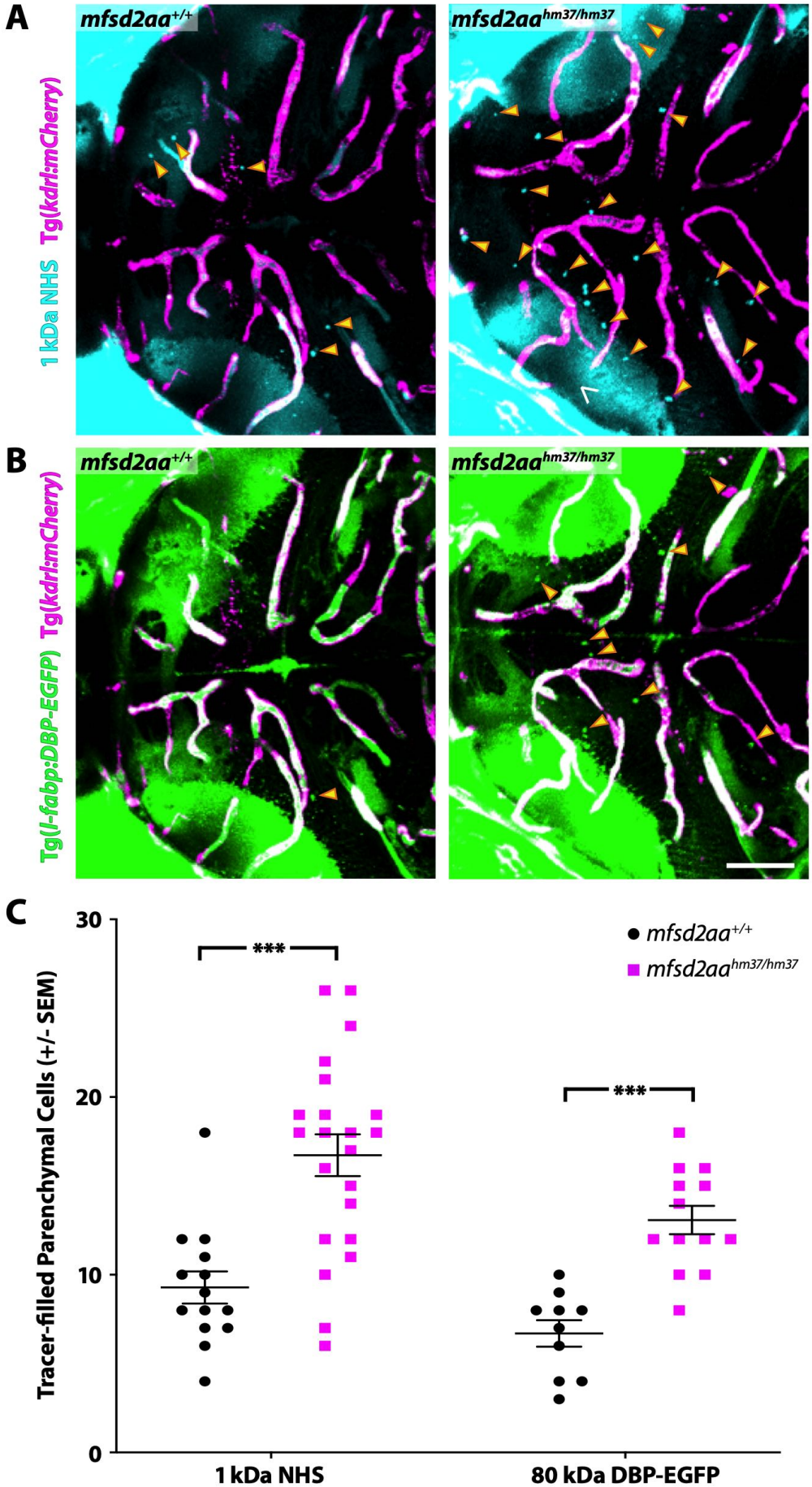
A
mfsd2aa+/+
mfsd2aahm37/hm37
1 kDa NHS Tg(kdrl:mCherry)
B
mfsd2aa+/+
mfsd2aahm37/hm37
Tg(l-fabp:DBP-EGFP) Tg(kdrl:mCherry)
C
Tracer-filled Parenchymal Cells (+/- SEM)
30
20
10
0
***
***
mfsd2aa+/+
mfsd2aahm37/hm37
1 kDa NHS
80 kDa DBP-EGFP

707

708 **Figure 4. *Mfsd2aa* mutants exhibit increased BBB permeability.** (A) Representative maximum
709 intensity projection images of the midbrain of wildtype and *mfsd2aa* mutants injected with a
710 fluorescent 1 kDa NHS tracer (turquoise) at 5 dpf. *Mfsd2aa* mutants have an increased number
711 of NHS-filled parenchymal cells (yellow arrowheads) that lie outside of the vasculature (magenta;
712 Tg(*kdrl:mCherry*)). (B) Representative maximum intensity projection images of the midbrain of
713 wildtype and *mfsd2aa* mutants expressing the fluorescently labelled 80 kDa transgenic serum
714 protein DBP-EGFP (green) at 5 dpf. *Mfsd2aa* mutants have an increased number of DBP-EGFP-
715 filled parenchymal cells (yellow arrowheads) compared to wildtype siblings. The scale bar
716 represents 50 μm. (C) Quantification of tracer-filled (NHS and DBP-EGFP) parenchymal cells in
717 the midbrain of wildtype (black) and *mfsd2aa* mutants (magenta). *Mfsd2aa* mutants have a
718 significantly increased number of tracer-filled parenchymal cells, both for the injected NHS (A)
719 and the endogenous transgene DBP-EGFP (B). Each individual fish measured is displayed as a
720 single point. The mean and the standard error are drawn as black lines. *** $p < 0.001$, ** $p < 0.01$.

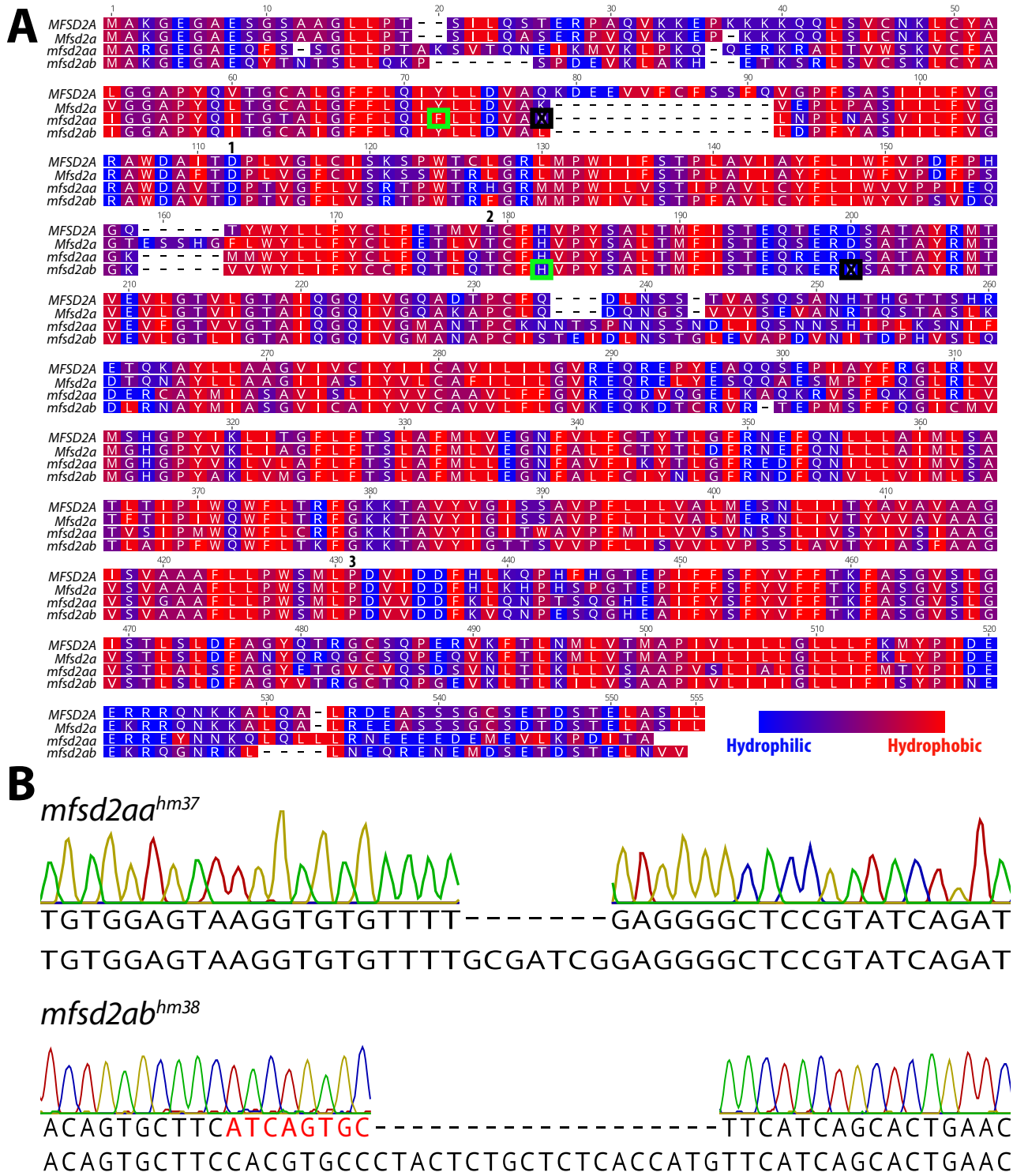
A
MFSD2A
Mfsd2a
mfsd2aa
mfsd2ab
Hydrophilic
Hydrophobic
B
mfsd2aa^hm37
TGTGGAGTAAGGTGTGTTTT-------GAGGGGCTCCGTATCAGAT
TGTGGAGTAAGGTGTGTTTTGCGATCGGAGGGGCTCCGTATCAGAT
mfsd2ab^hm38
ACAGTGCTTCATCAGTGC----------TTCATCAGCACTGAAC
ACAGTGCTTCCACGTGCCCTACTCTGCTCTCACCATGTTCATCAGCACTGAAC

721

722 **Figure 4 - Supplement 1. Zebrafish have 2 *Mfsd2a* paralogues, *mfsd2aa* and *mfsd2ab*.** (A)
723 Protein alignment of human MFSD2A, mouse Mfsd2a, zebrafish mfsd2aa, and zebrafish mfsd2ab
724 illustrated with a hydrophobicity scale. Red amino acids are hydrophobic and blue amino acids
725 are hydrophilic. Both zebrafish paralogues are highly similar to the human and mouse proteins.
726 Green boxes highlight the genetic lesions in (B) and the black boxes mark the predicted premature
727 stop codons caused by these mutations in *mfsd2aa*$^{hm37/hm37}$ and *mfsd2ab*$^{hm38/hm38}$ mutants.
728 Numbers mark amino acid residues with mutations that have been shown to impact Mfsd2a
729 function:1. Andreone et al., 2017, 2. Guemez-Gamboa et al., 2015, 3. Harel et al., 2018. (B)
730 Sanger sequencing of the *mfsd2aa*^{hm37} and *mfsd2ab*^{hm38} mutations. *Mfsd2aa*$^{hm37/37}$ mutants have
731 a 7 base pair deletion in exon 2 that is predicted to lead to a premature stop codon at amino acid
732 82 (A; black box). *Mfsd2ab*$^{hm38/hm38}$ mutants have an 8 base pair insertion (red letters) and a 19
733 base pair deletion in exon 5 that is predicted to lead to a premature stop codon at amino acid 175
734 (A; black box).

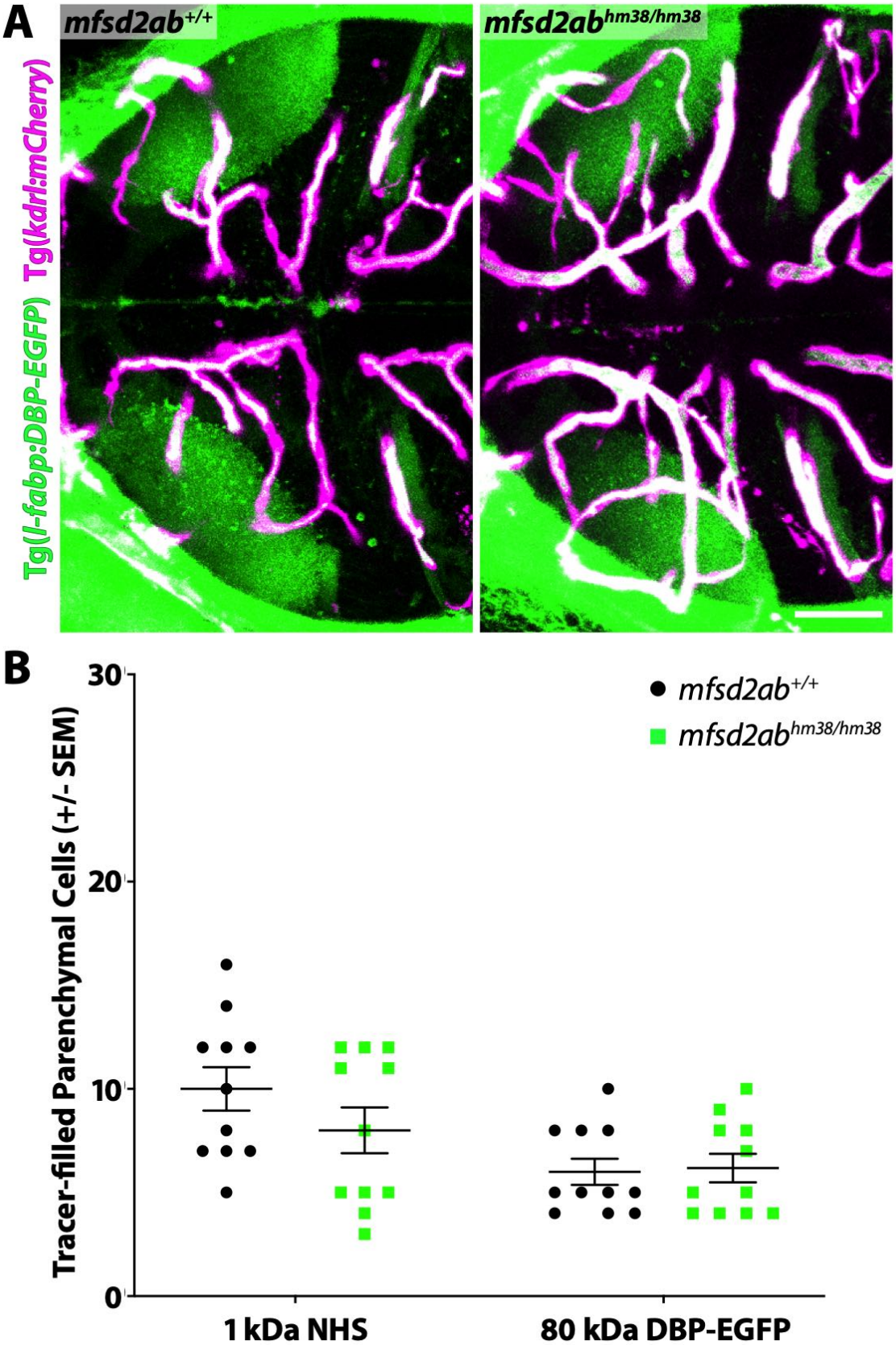
A
mfsd2ab+/+
mfsd2abhm38/hm38
Tg(kdrl:mCherry)
Tg(l-fabp:DBP-EGFP)
B
mfsd2ab+/+
mfsd2abhm38/hm38
Tracer-filled Parenchymal Cells (+/- SEM)
30
20
10
0
1 kDa NHS
80 kDa DBP-EGFP

735

736 **Figure 4 - Supplement 2. *Mfsd2ab* mutants do not have altered BBB permeability.** (A)
737 Representative maximum intensity projection images of the midbrain of wildtype and *mfsd2ab*
738 mutants expressing the fluorescently labelled 80 kDa transgenic serum protein DBP-EGFP
739 (green) at 5 dpf. *Mfsd2ab* mutants have a similarly low number of DBP-EGFP-filled parenchymal
740 cells compared to wildtype siblings. The scale bar represents 50 μm. (B) Quantification of tracer-
741 filled (NHS and DBP-EGFP) parenchymal cells in the midbrain of wildtype (black) and *mfsd2ab*
742 mutants (green). *Mfsd2ab* mutants display no significant barrier permeability defects, both for the
743 injected NHS and the endogenous transgene DBP-EGFP (A). Each individual fish measured is
744 displayed as a single point. The mean and the standard error are drawn in black.

A
mfsd2aa+/+; mfsd2ab+/+
B
mfsd2aahm37/hm37; mfsd2ab+/+
C
mfsd2aa+/+; mfsd2abhm38/hm38
D
mfsd2aahm37/hm37; mfsd2abhm38/hm38
E
DBP-filled Parenchymal Cells (+/- SEM)
30
20
10
0
****
****
mfsd2aa+/+; mfsd2ab+/+
mfsd2aahm37/hm37; mfsd2ab+/+
mfsd2aa+/+; mfsd2abhm38/hm38
mfsd2aahm37/hm37; mfsd2abhm38/hm38

746 **Figure 4 - Supplement 2. *Mfsd2aa$^{hm37/hm37}$; mfsd2ab$^{hm38/hm38}$* double mutants display similar**
747 **increased BBB permeability to *mfsd2aa$^{hm37/hm37}$* fish.** (A-D) Representative maximum intensity
748 projection images of the midbrain of wildtype (A; *mfsd2aa$^{+/+}$; mfsd2ab$^{+/+}$*), *mfsd2aa$^{hm37/hm37}$* single
749 mutants (B), *mfsd2ab$^{hm38/hm38}$* single mutants (C), and *mfsd2aa$^{hm37/hm37}$; mfsd2ab$^{hm38/hm38}$* double
750 mutants (D) expressing the fluorescently labelled 80 kDa transgenic serum protein DBP-EGFP
751 (green) at 5 dpf. *Mfsd2aa$^{hm37/hm37}$; mfsd2ab$^{hm38/hm38}$* double mutants display a similar level of
752 increased tracer-filled parenchymal cells (yellow arrowheads) to the *mfsd2aa$^{hm37/hm37}$* single
753 mutants. The scale bar represents 50 μm. (E) Quantification of DBP-EGFP-filled parenchymal
754 cells in the midbrain of wildtype (black), *mfsd2aa$^{hm37/hm37}$* mutants (magenta), *mfsd2ab$^{hm38/hm38}$*
755 mutants (turquoise), and *mfsd2aa$^{hm37/hm37}$; mfsd2ab$^{hm38/hm38}$* double mutants (green). Each
756 individual fish measured is displayed as a single point. The mean and the standard error are
757 drawn in black. **** $p < 0.0001$.
758

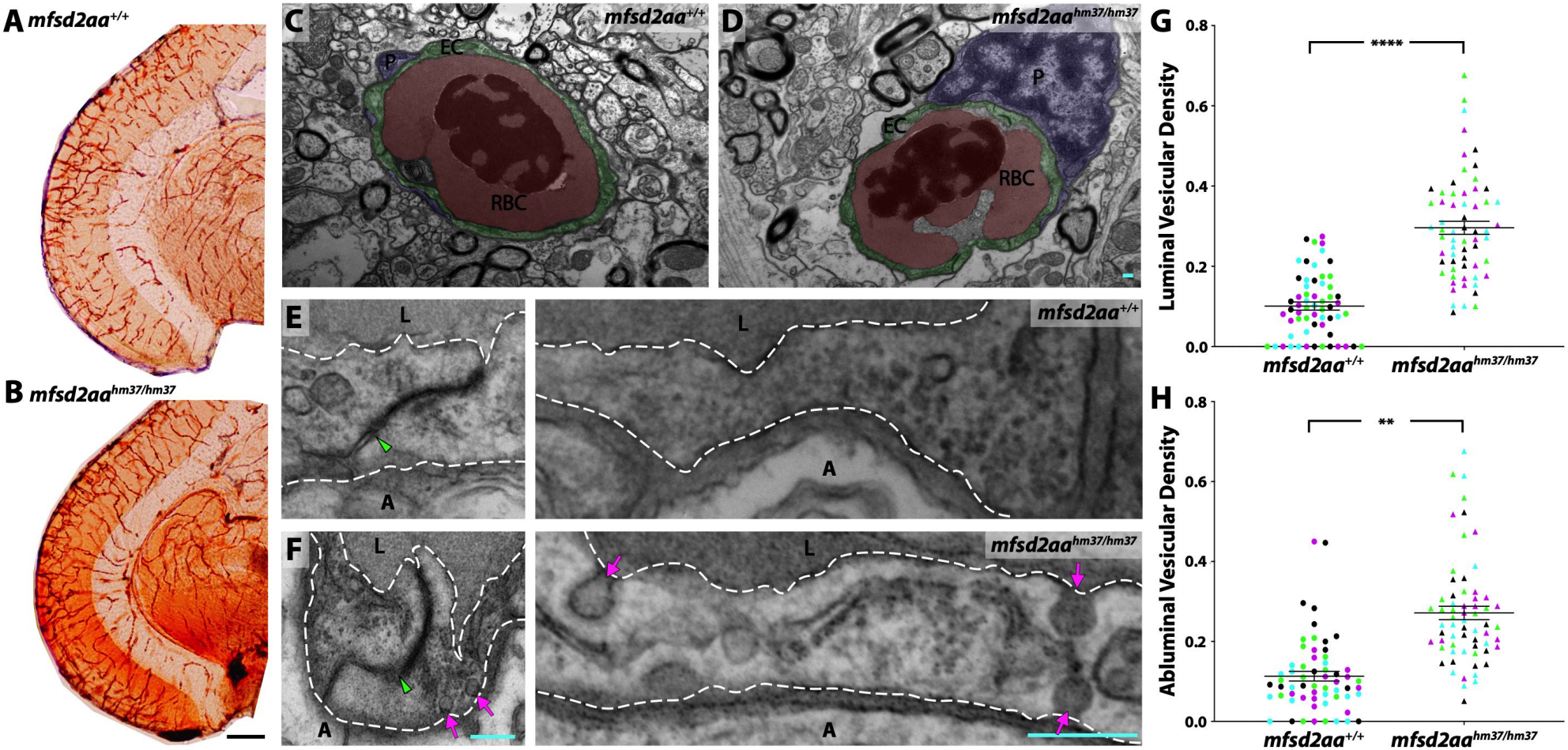
A mfsd2aa+/+
B mfsd2aahm37/hm37
C
mfsd2aa+/+
P
EC
RBC
D
mfsd2aahm37/hm37
P
EC
RBC
E
L
A
mfsd2aa+/+
L
A
F
L
A
mfsd2aahm37/hm37
L
A
G
Luminal Vesicular Density
0.0
0.2
0.4
0.6
0.8
****
mfsd2aa+/+
mfsd2aahm37/hm37
H
Abluminal Vesicular Density
0.0
0.2
0.4
0.6
0.8
**
mfsd2aa+/+
mfsd2aahm37/hm37

761 **Figure 5. M*fsd2aa* mutants exhibit increased transcytosis.** (A and B) Coronal sections of adult
762 midbrain after 30 minutes of HRP (brown) circulation in wildtype (A) and *mfsd2aa* mutant fish (B).
763 Wildtype adults confine the HRP within the blood vessels, but *mfsd2aa* mutants leak HRP into
764 the brain parenchyma. The scale bar represents 200 μm. (C and D) TEM images of individual
765 blood vessel cross-sections of adult wildtype (C) and *mfsd2aa* mutant fish (D). Endothelial cells
766 (EC) are pseudo-colored green, pericytes (P) are pseudo-colored purple and red blood cells
767 (RBC) are pseudo-colored red. (E and F) High magnification images of endothelial cells outlined
768 with white dashed lines of wildtype (E) and *mfsd2aa* mutants (F). The images are oriented with
769 the lumen (L) on top and the ablumen (A) on the bottom. *Mfsd2aa* mutants appear to have normal
770 tight junctions (green arrowhead) but elevated levels of luminal and abluminal vesicles (magenta
771 arrows). The scale bars represent 200 nm. (G and H) Quantification of the vesicular densities
772 both on the luminal (G) and abluminal (H) side of the endothelial cells reveals that *mfsd2aa*
773 mutants have increased vesicular densities. N=4 fish, each marked with a different color, with 15
774 blood vessels quantified for each fish. **** $p < 0.0001$, ** $p < 0.01$.

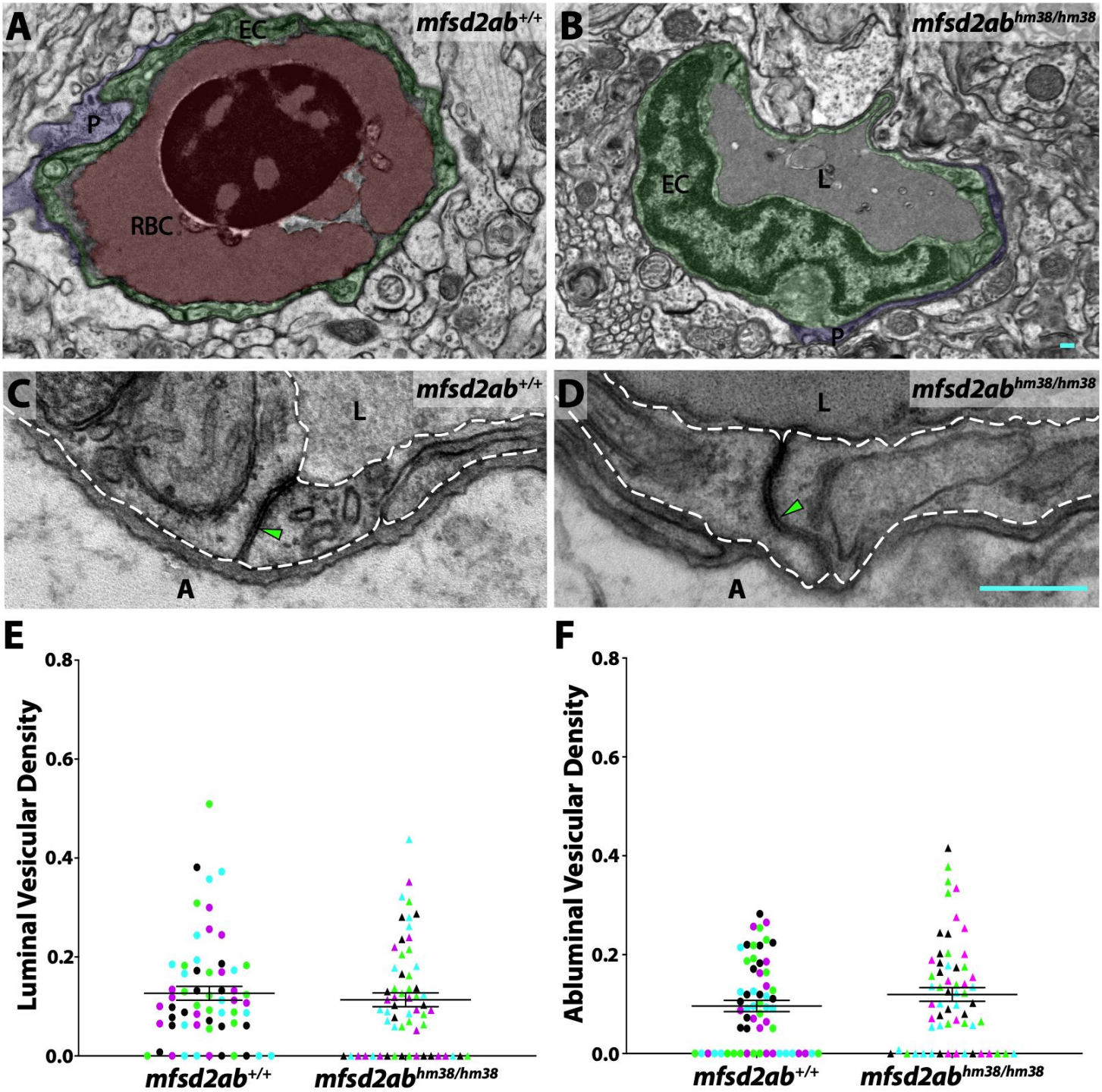
A
mfsd2ab+/+
EC
P
RBC
B
mfsd2abhm38/hm38
EC
L
P
C
mfsd2ab+/+
L
A
D
mfsd2abhm38/hm38
L
A
E
Luminal Vesicular Density
0.8
0.6
0.4
0.2
0.0
mfsd2ab+/+
mfsd2abhm38/hm38
F
Abluminal Vesicular Density
0.8
0.6
0.4
0.2
0.0
mfsd2ab+/+
mfsd2abhm38/hm38

775

776

777 **Figure 5 - Supplement 1. M*fsd2ab* mutants exhibit normal vascular maturation.** (A and B)
778 TEM images of individual blood vessel cross-sections of adult wildtype (A) and *mfsd2ab* mutants
779 (B). Endothelial cells (EC) are pseudo-colored green, pericytes (P) are pseudo-colored purple
780 and red blood cells (RBC) are pseudo-colored red when present in the lumen (L). (C and D) High
781 magnification images of endothelial cells outlined with white dashed lines of wildtype (C) and
782 *mfsd2ab* mutants (D). The images are oriented with the lumen (L) on top and the ablumen (A) on
783 the bottom. *Mfsd2ab* mutants appear to have normal tight junctions (green arrowhead) and levels
784 of luminal and abluminal vesicles. The scale bars represent 200 nm. (E and F) Quantification of
785 the vesicular densities both on the luminal (E) and abluminal (F) side of the endothelial cells
786 reveals that *mfsd2ab* mutants have similar vesicular densities to wildtype siblings. N=4 fish, each
787 marked with a different color, with 15 blood vessels quantified for each fish.